

DIGITAL ACCESS TO SCHOLARSHIP AT HARVARD
DASH.HARVARD.EDU

HARVARD LIBRARY


Single-cell transcriptomic profiling of the aging mouse brain

Citation

Ximerakis, Methodios, Scott L. Lipnick, Brendan T. Innes, Sean K. Simmons, Xian Adiconis, Danielle Dionne, Brittany A. Mayweather, et al. 2019. Single-Cell Transcriptomic Profiling of the Aging Mouse Brain. Nature Neuroscience 22, no. 10: 1696–1708.

Published version

https://doi.org/10.1038/s41593-019-0491-3

Link

http://nrs.harvard.edu/urn-3:HUL.InstRepos:42659942

Terms of use

This article was downloaded from Harvard University's DASH repository, and is made available under the terms and conditions applicable to Other Posted Material (LAA), as set forth at

https://harvardwiki.atlassian.net/wiki/external/NGY5NDE4ZjgzNTc5NDQzMGIzZWZhMGFlOWI2M2EwYTg

Accessibility

https://accessibility.huit.harvard.edu/digital-accessibility-policy

Share Your Story

The Harvard community has made this article openly available.
Please share how this access benefits you. Submit a story

Single-cell transcriptomic profiling of the aging mouse brain

Methodios Ximerakis[1,2,3,8,*], Scott L. Lipnick[1,2,3,4,8], Brendan T. Innes[5], Sean K. Simmons[3], Xian Adiconis[3], Danielle Dionne[3], Brittany A. Mayweather[1,2], Lan Nguyen[3], Zachary Niziolek[6], Ceren Ozek[1,2], Vincent L. Butty[7], Ruth Isserlin[5], Sean M. Buchanan[1,2], Stuart S. Levine[7], Aviv Regev[3], Gary D Bader[5], Joshua Z. Levin[3], Lee L. Rubin[1,2,3,*]

[1]*Department of Stem Cell and Regenerative Biology, Harvard University, Cambridge, MA 02138, USA*

[2]*Harvard Stem Cell Institute, Cambridge, MA 02138, USA*

[3]*Broad Institute of MIT and Harvard, Cambridge, MA 02142, USA*

[4]*Department of Biomedical Informatics, Harvard Medical School, Boston, MA 02115, USA*

[5]*The Donnelly Centre, University of Toronto, Toronto, ON M5S 3E1, Canada*

[6]*Bauer Core, FAS Division of Science, Harvard University, Cambridge, MA 02138, USA*

[7]*BioMicro Center, Massachusetts Institute of Technology, Cambridge, MA 02139, USA*

[8]*These authors contributed equally to this work*

[*]*Correspondence: M.X. (methodios_ximerakis@harvard.edu); L.L.R. (lee_rubin@harvard.edu)*

ABSTRACT

The mammalian brain is complex, with multiple cell types performing a variety of diverse functions, but exactly how the brain is affected with aging remains largely unknown. Here we performed a single-cell transcriptomic analysis of young and old mouse brains. We provide a comprehensive dataset of aging-related genes, pathways and ligand-receptor interactions in nearly all brain cell types. Our analysis identified gene signatures that vary in a coordinated manner across cell types and gene sets that are regulated in a cell type specific manner, even at times in opposite directions. Thus, our data reveal that aging, rather than inducing a universal program, drives a distinct transcriptional course in each cell population. These data provide an important resource for the aging community and highlight key molecular processes, including ribosome biogenesis, underlying aging. We believe that this large-scale dataset, which is publicly accessible online (aging-mouse-brain), will facilitate additional discoveries directed towards understanding and modifying the aging process.

INTRODUCTION

Aging, the time-dependent functional decline of organs and tissues, is the biggest risk factor for many diseases, including several neurodegenerative and cardiovascular disorders [1,2].

Characterizing aging-related molecular and cellular changes will provide insights into this complex process and highlight opportunities to slow or reverse its progression, thereby helping to prevent or treat aging-associated pathologies. That this might be achievable is supported by a plethora of studies using model organisms demonstrating that not only lifespan, but also the integrity of multiple tissues, can be regulated by discrete molecular modifications [3-5].

Towards the goal of achieving a broader understanding of aging-related changes and deciphering the molecular mechanisms that accompany brain aging, transcriptomic studies in model organisms and humans have been at the forefront of experiments. However, these studies generally utilize aggregated RNA from either mixed cell populations [6-12] that may vary in distinct ways with age, or cell populations purified using known markers [13-22], which themselves may also change during aging. Therefore, despite the successful identification of major aging-related genes and pathways, prior transcriptomic analyses have not resolved the common aging-related changes experienced across all brain cells from those that may be cell-type specific. Thus, there is a need to elucidate how individual cell types are affected by aging and to clarify if the process of aging follows a similar blueprint in all cell types or whether certain cell types have unique transcriptional changes. This will be critical in determining whether aging at the tissue level is a global process, if it results from specific changes in certain cell types that culminate in loss of function and deterioration, or a combination of both [23]. This information may also help the design of effective aging-related therapeutics that are targeted either narrowly, affecting only certain cell types, or more broadly, affecting all cells.

In this study, to begin to address these issues, we employed single-cell RNA sequencing to profile and compare the cellular composition and transcriptomes of young and old mouse brains. This is the first large-scale transcriptomic analysis of aging for the vast majority of individual brain cell types. For all the major cell populations identified, we provide a comprehensive dataset of genes and pathways whose transcriptional profiles change with aging. Our computational analysis suggests that cells in the brain do not change with aging identically, indicating that, while overlapping signatures exist, the cellular consequences of aging are not universal. Given that cell non-autonomous changes are also known to regulate aging-dependent changes [3,4], we also detail ligand-receptor interactions among nearly all the cell types in the brain that are modified by aging. Overall, this study provides a rich resource that can facilitate the interrogation of the molecular underpinnings and cellular basis of the aging process in the mouse brain.

RESULTS

Identification of cell types

To gain new, more precise, insights into the effects of aging, we employed unbiased high-throughput single-cell RNA sequencing (scRNA-seq) to examine the transcriptional profiles of young and old mouse brains (Fig. 1A). Because the dissociation of mammalian adult brains is challenging due to the complexity of the tissue involving a very dense intercellular space, including an extensive neuronal network insulated by myelin sheaths, we first developed a new dissociation protocol that enables the isolation of healthy and intact cell suspensions that are representative of both young and old mouse brains (see details in Supplementary Methods).

We then analyzed the transcriptomes of 50,212 single cells (24,401 young and 25,811 old) derived from the brains of 8 young (2-3 months) and 8 old (21-23 months) mice (Supplementary Fig. 1-2). We first aggregated transcriptionally similar cells, using an established clustering algorithm [24,25]. Next, we removed clusters likely to be of low quality, resulting from debris, doublets/multiplets and dead cells (Supplementary Fig. 3), and employed other critical quality control steps as described in the Supplementary Methods (Supplementary Fig. 4). Ultimately, our analysis led to the identification of 37,069 cells (Supplementary Fig. 5A), representing 25 cell types (Fig. 1B) with distinct expression profiles (Fig. 1C-D and Supplementary Fig. 6): oligodendrocyte precursor cells (OPC), oligodendrocytes (OLG), olfactory ensheathing glia (OEG), neural stem cells (NSC), astrocyte-restricted precursors (ARP), astrocytes (ASC), neuronal-restricted precursors (NRP), immature neurons (ImmN), mature neurons (mNEUR), neuroendocrine cells (NendC), ependymocytes (EPC), hypendymal cells (HypEPC), tanycytes (TNC), choroid plexus epithelial cells (CPC), endothelial cells (EC), pericytes (PC), vascular smooth muscle cells (VSMC), hemoglobin-expressing vascular cells (Hb-VC), vascular and leptomeningeal cells (VLMC), arachnoid barrier cells (ABC), microglia (MG), monocytes (MNC), macrophages (MAC), dendritic cells (DC), and neutrophils (NEUT). Cell counts and other sequencing metrics for each identified cell type are shown in Fig. 1E and Supplementary Fig. 5B-E.

Identification of cell subtypes and states

To reveal heterogeneity within each population, we grouped the aforementioned cell types into 6 classes based on their expression profile, lineage, function and anatomical organization (oligodendrocyte lineage, astrocyte lineage and stem cells, neuronal lineage, ependymal cells, vasculature cells, and immune cells) (Supplementary Fig. 7) and employed another round of clustering. This subsetting of the data enabled us to highlight more subtle changes within the classes without the impact of variation due to inclusion of drastically different cell identities. This secondary analysis identified dozens of different cell subtypes and states reflecting distinct functional, maturational and regional cell identities (Supplementary Fig. 8-9). These cell identities are in line with recent scRNA-seq studies [26-42], whose purpose was to identify novel and distinct cell types/subtypes and create detailed atlases of the developing and adult mouse brain (see details in Supplementary Fig. 8). This

allowed us to generate a comprehensive dataset of gene expression profiles for all the experimentally validated cell populations from both young and old brains at high resolution (Supplementary Tables 1 and 2). It also permitted us to identify specific markers that distinguish each type regardless of age (Supplementary Table 3).

Aging-related effects on cell-to-cell transcriptional variability and cellular composition

We found that cell identity is largely preserved in old brains as indicated by unbiased clustering where all clusters represent cells of all animals from both ages (Supplementary Fig. 4C). Furthermore, the quality of data generated from both young and old cell types appears similar, with each having comparable numbers of unique molecular identifiers (UMI) and detected genes (Supplementary Fig. 5C, E). Next, we compared the coefficient of variation (CV) of expression for all the transcribed genes (Supplementary Fig. 10A), only the mitochondrially-encoded genes (Supplementary Fig. 10B), or only the ribosomal protein genes (Supplementary Fig. 10C). We observed differences in the variability of transcription between young and old cells in many cell types. However, the directionality of change was not identical among cell types, providing evidence that aging is not broadly associated with increased transcriptional variation [43].

Then, by investigating the abundance of each cell type, we found that cellular composition was largely consistent across both young and old brains (Fig. 2A and Supplementary Table 4). Nonetheless, we were able to confirm the previously reported aging-related decline of OPC [44], NRP [45,46] and ImmN [46,47]. (Fig. 2A), and to reveal potentially interesting but not statistically significant population shifts within certain subtypes of OPC, OLG, ASC, mNEUR and MG (Supplementary Fig. 11; see also details in Supplementary Fig. 8). Of note, although the estimated percentages for each cell type do not necessarily reflect their actual proportions in the mouse brain, mainly due to differences in their sensitivity to tissue dissociation, the observed changes in cell type ratios appear to reflect a real biological effect.

Identification of aging-related genes

We then investigated the breadth of transcriptional changes that occur in the mouse brain with aging by performing differential gene expression (DGE) analysis between young and old cell types and neuronal subtypes (Supplementary Table 5). Of the 14,699 total detected genes, 3,897 were significantly affected by aging in at least one cell type (FDR<0.05). When the magnitude of change in expression was also considered, 1,113 genes passed the 10%-fold-change (FC) threshold (Fig. 2B and Supplementary Table 6). Interestingly, of those, 1,027 exhibited the same directionality regardless of the cell type identity (531 upregulated and 496 downregulated), while the direction of change in the expression of 86 genes was different across cell populations (discussed further below; Supplementary Table 6). As described in Supplementary Methods, our ability to identify genes whose

transcription changes significantly with aging and the calculation of fold-change is dependent on several factors, including the number of cells within each population, the level of transcription, and the algorithm for analysis.

Identification of shared and cell-type specific aging signatures

To ensure the validity of these aging signatures, we first started broadly and compared our data with past transcriptomic studies of the mouse aging brain [6,8,48]. To more effectively compare datasets, we aggregated all of our sequenced cells, thereby recreating a traditional whole brain profile similar to what might be observed using bulk sequencing (Supplementary Tables 2 and 5). As expected, this analysis verified previously identified top aging-related genes (such as *Apod, B2m*, *C1qa*, *C4b, Ctss, Il33, Rpl8*). Moreover, due to the increased sensitivity of the techniques used in our study compared to past ones, we were able to identify a set of aging-related genes not reported previously (such as *Apoc1*, *Caly*, *Cxcl12, Nell2, Ybx1*; see Supplementary Table 5). These changes could have been masked in past studies due to their limited expression levels or variations in less abundant cell types. Importantly, our single cell DGE data enabled us to build on these results to identify from which cell types these aging signatures arose. For example, *Ctss,* while highly transcribed in all immune cells (MG, MAC, MNC, DC; see Supplementary Table 2), was only significantly changed with aging in MG (Supplementary Table 5). Another example is *Nell2,* which is mostly transcribed in neuronal lineage cells and OEG (Supplementary Table 2), but its levels changed with aging only in OEG (Supplementary Table 5).

We then focused our analysis on 11 major cell populations that exhibited the greatest number of differentially regulated genes (see Fig. 2B). By comparing the DGE data from these cell populations (Fig. 2C and Supplementary Fig. 12), we were able to distinguish both shared and cell-type specific aging signatures. Supplementary Table 6 presents a matrix that specifies the genes that changed significantly in each cell type.

Fig. 2D presents selected top aging-related genes that are shared across multiple cell types. The majority of the most commonly aging-upregulated genes were ribosomal protein genes (such as *Rpl6*), lncRNA genes (such as *Malat1*) and immunoregulatory/inflammatory genes (such as *B2m*). The most commonly aging-downregulated genes were mitochondrial respiratory chain complex genes (such as *mt-Nd1*), glycolysis-related genes (such as *Aldoc*), genes encoding selenoproteins (such as *Sepw1*) and tetraspanins (such as *Tspan7*) (Fig. 2D and Supplementary Table 6).

A subset of genes representing cell-type specific aging signatures are highlighted in Fig. 2E. Interestingly, these data revealed that certain genes that are traditionally used as cell type specific markers change with aging, such as the decrease of *Mog* in OLG and *Csf1r* in MG, and the increase of *Cxcl12* in EC (Fig. 2E and Supplementary Tables 5 and 6). Conversely, we observed that other classic cell type marker genes change with aging in other cell types. For example, *Gfap,* which is highly transcribed and enriched in the astrocyte lineage and

stem cells (Supplementary Table 2), was found as one of the genes that increased the most in EPC (Fig. 2E and Supplementary Tables 5 and 6).

We next sought to validate certain shared and cell type unique aging-related gene expression changes. As shown in Fig. 3A, we were able to verify transcriptional changes in the shared aging-related genes *Rpl6*, *Malat1* and *Meg3* by *in situ* hybridization. We also confirmed the cell type specific aging-related changes of genes such as *B2m*, *Csf1r, Ctss*, *Cxcl12* and *Sparc* by bulk RNA-seq and qRT-PCR analysis of FACS-purified $CD31^+$ (EC), $CD11b^+$ (MG) and $ACSA2^+$ (ASC) cells (Fig 3B-C and Supplementary Fig. 13). Additionally, to further determine if our transcriptomic approach faithfully captured changes at the protein level, we performed immunohistochemistry. As shown in Fig. 3D, we again observed the specific aging-related downregulation of SPARC in MG and the global aging-related increase of IL33 that is mostly expressed by OLG (Supplementary Fig. 14), as revealed by our scRNA-seq analysis (Fig. 2E and Supplementary Table 2) and by others [31,34].

Identification of bidirectional aging signatures

Analysis of our sequencing dataset also revealed individual genes with opposite regulation among different cell types (Supplementary Fig. 15 and Supplementary Table 6). For example, the tetraspanin *Cd9* was downregulated in OPC and ASC but upregulated in EC and MG. This bidirectional aging signature was confirmed between OPC and MG by dual fluorescence *in situ* hybridization (Fig. 4A-B). Another example of bidirectional changes with aging is *Cldn5,* which is often used as a marker for EC, but it is also highly transcribed in OEG (Supplementary Table 2). We found aging-related downregulation of *Cldn5* in EC but upregulation in OEG (Supplementary Table 5). Notably, when its levels were measured in the whole brain, changes were minimal (Supplementary Tables 2 and 5), further highlighting why certain aging-related changes were masked in previous bulk sequencing studies.

Similarly, we found large gene sets, such as ribosomal protein genes, that were discordant between cell types (Supplementary Fig. 15B and Supplementary Table 6). As mentioned above, many ribosomal protein genes were found among the top shared aging-upregulated genes across major cell populations (Fig. 2D and Supplementary Table 6), but a subset of these genes also exhibited differential regulation/directionality with aging in certain cell types (Supplementary Fig. 15B). For example, *Rps23* was found to be downregulated in OPC and ASC, but upregulated in mNEUR, EC and MG. This differential aging-related transcriptional signature was confirmed in OPC and MG by dual fluorescence *in situ* hybridization (Fig. 4C-D).

Interestingly, when we examined the expression profile of all genes encoding ribosomal proteins across major cell populations, we found two distinct and divergent patterns. As shown in Fig. 5A (see also Supplementary Table 6), both OPC and ASC were found to downregulate a fraction of their ribosomal protein genes with aging, while the other cell

types upregulated their expression. These patterns of expression were also detected when neuronal subtypes were compared, where GABA and GLUT neurons exhibited upregulation of their ribosomal protein genes with aging, while DOPA neurons exhibited downregulation (Supplementary Table 5). To validate these broad bidirectional aging-related signatures, we examined ribosomal protein gene expression in FACS-purified ACSA2$^+$ (ASC), CD31$^+$ (EC) and CD11b$^+$ (MG) cells. As shown in Fig. 5B-C, bulk RNA-seq reproduced the scRNA-seq data for a subset of ribosomal protein genes, highlighting their potentially distinct responses to aging.

Identification of aging-related pathways

Next, we investigated changes in aging-related cellular pathways and processes by performing gene set enrichment analysis (GSEA) [49]. GSEA has increased sensitivity compared to DGE analysis as it aggregates information from broad sets of genes that are presumed to be functionally related. As such, we were also able to include cell types and neuronal subtypes with limited cell numbers that did not show significant aging-related changes by DGE analysis. This approach revealed the existence of many shared and cell-type specific aging-related pathways across the examined cell populations (Fig. 6 and Supplementary Tables 7 and 8). In total, 451 pathways (1,142 GSEA terms) changed significantly ($p<0.05$ & $q<0.25$); 234 were expressed in at least 2 cell types, while the remaining 217 were unique for specific cell populations. Of those aging-related pathways, 339 exhibited the same directionality regardless of cell type (195 were upregulated and 144 downregulated), while the directions of change in the remaining 112 varied across cell types (Supplementary Table 8). The most common aging-related pathways were those associated with cellular respiration, protein synthesis, inflammatory response, oxidative stress, growth factor signaling, and neurotrophic support (Fig. 6 and Supplementary Table 8). As expected, GSEA showed that the aging process entails many biological changes in mNEUR that were in common across its major subtypes. These include the impairment of key metabolic pathways, the dysregulation of ion homeostasis and the disruption of neurotransmission (Supplementary Tables 7 and 8), all of which have been very well documented in the literature [5].

Here, we highlight changes in EC and EPC, two understudied, but important, brain cell populations, that form the barriers that isolate the brain parenchyma from factors circulating in blood and cerebrospinal fluid. GSEA showed that EC exhibit numerous aging-regulated cellular pathways and biological processes, such as the aging-related induction of senescence, hypoxia signaling and response to ketone signaling, and the aging-related reduction of xenobiotic metabolism, lipid metabolism and hormone processing (Supplementary Fig. 16A and Supplementary Tables 7 and 8). In EPC, there was a notable upregulation of interferon-induced signaling (Supplementary Fig. 16B and Supplementary Tables 7 and 8) that aligns with the induction of certain interferon-stimulated genes (like *Ifitm3*) just as found in the DGE analysis (Supplementary Tables 5 and 6). The aging-related

upregulation of interferon-stimulated genes and other aging-induced genes was also seen by qRT-PCR in FACS-purified EPC (Supplementary Fig. 17). This suggests that an aging-induced inflammatory response may extend to these cells, and appears similar to what it has been previously reported for the choroid plexus epithelium [50].

Importantly, GSEA also points to ribosome biogenesis as a biological process exhibiting differential regulation with aging across different cell types and neuronal subtypes, beyond what we found based on DGE analysis alone (Supplementary Tables 7 and 8). In particular, even employing stringent significance criteria, the vast majority of brain cell types were seen to exhibit an aging-related upregulation of genes encoding ribosomal subunits, while three types of stem/progenitor cells (NSC, NRP, OPC) showed downregulation (Fig. 6, Supplementary Fig. 18 and Supplementary Table 8).

Identification of aging-related changes in intercellular communication

Finally, our single-cell transcriptomics data provides the ability to explore how aging-driven changes in gene expression might affect intercellular communication within the brain. By leveraging the transcriptional profiles of each cell population, we built a comprehensive intercellular network of potential ligand-receptor interactions among nearly all the identified brain cell types. We then enriched this network with data from our DGE analysis to mark all those interactions that were found to change with aging at the ligand or receptor level. To facilitate the visualization and exploration of these data, we created an online interactive data viewer that can also be downloaded as an R package (see details in Supplementary Methods).

Here we highlight the ligand-receptor changes in EC (Fig. 7), not only because they exhibited a variety of aging-related changes, as mentioned above (see Fig. 2B-C and Supplementary Fig. 16A), but also because they possess the unique ability to interact directly with factors synthesized in the brain and with those secreted by peripheral tissues into the circulation. Network analysis showed that both cystatin C (*Cst3*; an aging-downregulated gene), and stromal cell-derived factor 1 (*Cxcl12*; an aging-upregulated gene) (see Fig. 3B), which have been previously linked to multiple pathologies [51-54], are mediators of crosstalk between vascular cells and many brain cell types (Fig. 7). This signifies that their aging-related changes may modulate, either synergistically or separately, important, still to be identified aging-related processes occurring in the brain parenchyma.

DISCUSSION

The transcriptomic database reported here is the first to examine the aging process in the mammalian brain at a single-cell level. In this study, we first investigated the cellular complexity of the mouse brain and showed that cell identity and composition is generally maintained with aging. More specifically, we found that the numbers of cells within most of

the cell types did not change radically with age, when quantified as a fraction of total brain cells, which is in line with previous findings [55-59]. Nonetheless, we did observe the previously reported aging-related decline of certain cell populations, such as NRP [45,46]. Of note, it seems possible that additional work focused on this issue might reveal additional changes in subtypes of cells, particularly those occurring in specific regions of the brain.

We then compared young and old cells and observed a noticeable aging-related cell-to-cell transcriptional variation within certain cell populations. However, our data did not show a universal aging-related change in transcriptional variability across all cell types. That is, gene transcription in particular cell populations does not necessarily become more variable with aging. This is in line with Warren et al. [60], but in contrast to other studies that suggested increased transcriptional variability as a common feature of aging [43,61].

By aggregating all of our sequenced single cells and performing DGE analysis comparable to what was done in prior bulk sequencing studies, we validated many of the previously identified aging-related genes [6,8,48] and extended the list to include numerous additional gene signatures. We then utilized single cell type DGE analyses to reveal the primary cell type(s) generating these signatures. The fine resolution provided by scRNA-seq further allowed us to detect changes in specific cell populations that would otherwise be masked by bulk sequencing techniques. More specifically, single cell type DGE analyses yielded a large number of aging-related genes that are: (a) commonly regulated among cell types, (b) specific to certain cell types and (c) discordant between cell types. To the best of our knowledge, only a small fraction of the genes reported here have been previously associated with brain aging.

Interestingly, our data analysis revealed different patterns of aging across cell populations. We found that certain aging-related genes and pathways are differentially regulated across cell types. For example, we provide evidence that, with aging, expression of ribosomal protein genes is regulated in opposite directions among groups of cell types and among neuronal subtypes. Data from both DGE and pathway analyses showed that most of the brain cell types exhibited an aging-driven upregulation of ribosomal protein genes, while those exhibiting the opposite regulation include important stem/progenitor cell populations. This paradoxical bidirectional regulation of ribosomal protein genes with aging is noteworthy.

Over the past few years, it has been clearly shown that the attenuation of protein synthesis by dietary restriction or genetic manipulation of translation-associated genes, including those encoding ribosomal subunits, increases the lifespan of multiple species [62]. Notably, the down-regulation of ribosomal protein genes and bulk protein synthesis has been long considered as a hallmark of aging [63,64]. It appears that the aging-driven down-regulation of ribosomal protein genes had been widely accepted, mostly based on transcriptomic studies

in yeast [65,66]. However, several studies in other model organisms and humans have presented conflicting results [7,12,67-74]. Zahn et al. reported an aging-driven upregulation of ribosomal protein genes in human brain and muscle tissues [48] and, in a later study, reported an aging-driven upregulation of ribosomal protein genes in mouse neuronal tissues [7] with a downregulation of the same genes in multiple non-neuronal tissues [7]. Moreover, recently published transcriptomic studies showed an aging-related downregulation of ribosomal protein genes in both ASC [17] and NSC [75], and an upregulation in MG of both aged [18,76] and diseased brains [76-78]. Intriguingly, a very recent study reported increased ribosome biogenesis and activity as hallmarks of premature aging in human fibroblasts [79]. A possible explanation for this is that cells with different metabolic demands are affected differently by aging, thus inducing alternative feedback loops to partially compensate for loss of translational efficiency and protein synthesis. Another explanation is that certain cell populations may start producing different types and/or levels of specialized ribosomes [80] tailored to their translational needs to cope with the metabolic changes induced by aging.

Collectively, these data indicate that the aging process may not be identical in all cell types, which is in line with our findings and with a recent transcriptome analysis of the *Drosophila* brain that showed a differential aging trajectory in the transcriptional profile of neurons and glial cells [72]. In short, it is not yet clear whether the regulation of ribosomal protein genes and other translation-associated genes is causative of aging or the consequence of physiological changes accompanying aging, or both depending on species, tissue and cell type. However, our work demonstrating that ribosome biogenesis is one of the aging-related pathways that is differentially regulated across different cell types may help to reconcile seemingly conflicting studies.

Lastly, we created a roadmap of intercellular communication in the brain by generating detailed information on ligand-receptor interactions that change with aging across nearly all brain cell types. This is also of high importance as recent findings from our lab [81] and others [50,82-84] have shown that certain secreted factors, either derived from brain parenchyma or blood, are able to modulate brain aging, degeneration and rejuvenation. Thus, the discovery of novel factors, their source, and their targets are emerging areas of importance in the aging field and will be crucial for understanding brain physiology in both health and disease [4]. We foresee the extension of this network by including data from blood proteomic analyses and transcriptomic data from both mouse disease models and heterochronic parabiosis experiments [81], to generate additional data that may help in identifying novel therapeutic targets for treating functional defects in the brain brought on by aging and disease.

Our findings, in agreement with recent studies, highlight the sensitivity and power of single-cell transcriptomics not only to reveal differences in cell identities, but also to reveal

changes within individual cell types after different treatments and conditions [30,33,34,85], including organismal aging [18,20,21,71-73]. As single-cell sequencing technologies continue to mature, some of the technical and experimental limitations that we encountered will be improved upon. These include: (a) potential sampling problems resulting from the enzymatic dissociation of the brain that may be overcome using single-nuclei sequencing approaches [27,86]; (b) potential age-associated biases in response to dissociation, cell encapsulation, and other procedures that might drive transcriptional differences between experimental groups; (c) the relatively small number of cells sequenced compared to the total size of the brain, restricting the comparative analyses to more abundant cell populations; (d) the relatively shallow depth of sequencing limiting the analysis to highly transcribed genes; and (e) the lack of full-length splicing isoform profiling that could be enabled using other methods [87]. Our data could not also reveal potentially important aging-driven regional changes [22,88] that may be resolved using spatial mapping sequencing approaches [89], and sex-specific gene expression variations as only whole brain preparations of male mice were analyzed.

Nonetheless, our work identified aging-related changes in nearly all mouse brain cell types and revealed different patterns of aging across different cell populations, many of which we validated in this study. Thus, while there may be hallmarks of aging that occur in most cell types, such as mitochondrial dysfunction and loss of proteostasis [1,2,5,63], our data argue against the hypothesis that aging induces a single universal molecular program in all cells and tissues [23]. However, we note that the aging process, now thought to begin soon after birth, may occur gradually or in discrete steps depending on complex interactions among cells in the brain, and ways in which these interactions modified by extrinsic factors, such as stress and exercise. Thus, future studies studying gene expression changes along a continuum, by examining additional timepoints, will help to reveal the precise aging trajectories for each cell and gene, and to distinguish changes that are causative of aging from those that change as a consequence of aging. Future studies will also assist in deciphering the exact molecular mechanisms and dynamics by which cell types, tissues and organisms respond to normal aging.

Collectively, as a resource to the aging community, we provide a comprehensive dataset of genes, pathways and ligand-receptor interactions with aging-related variation for all the cell types identified. We expect that, beyond the valuable exploration of aging signatures and novel insights regarding the aging process, our data will be used as a reference for a series of other applications. For example, we showed that numerous putative cell specific marker genes change with aging. Thus, the purification or investigation of cells based on single discriminatory markers maybe faulty in the context of aging. Similarly, our data revealed that the transcript levels of certain housekeeping genes change with aging in many cell types, which could confound some quantitative analyses.

Finally, we expect that these data will help to advance a variety of efforts towards understanding and modulating the aging process and exploring molecular and cellular therapeutic targets for aging-related neurodegenerative diseases. Furthermore, as mentioned above, we hope that our data will serve as a benchmark from which to carry out future studies with higher spatial and temporal resolution.

ACKNOWLEDGEMENTS

We would like to acknowledge Tomotaka Okino and his team at Ono Pharmaceuticals for fruitful discussions and useful suggestions during the progress of this work. We are grateful to Francesca Rapino, Natalia Rodriguez-Muela, Kathleen Pfaff, Adam Freeman, and Jane LaLonde for their helpful advice in different aspects of our work and/or for reviewing the manuscript. We also thank the stuff members of the Harvard Bauer Core Facility, the Harvard Center for Biological Imaging and the Harvard Stem Cell and Regenerative Biology Histology Core for their technical advice and assistance. The work was supported by Ono Pharmaceutical Co., Ltd (L.L.R.), the Stanley Center for Psychiatric Research and the Klarman Cell Observatory (J.Z.L). The funders had no role in the study design, experiments performed, data collection, data analysis and interpretation, or preparation of the manuscript.

AUTHOR CONTRIBUTIONS

M.X., S.L.L., S.M.B. and L.L.R. conceived the study; M.X., S.L.L., S.M.B., J.Z.L. and L.L.R. designed the study; M.X., X.A., D.D. and L.N. performed the single cell RNA-seq experiments; S.L.L., S.K.S. and J.Z.L. processed the single cell RNA-seq data; M.X. and S.L.L. analyzed the single cell RNA-seq data; B.T.I. and G.D.B created the ligand-receptor interaction network; M.X. and V.L.B. performed the bulk RNA-seq experiments; S.L.L and V.L.B. processed the bulk RNA-seq data; M.X. and S.L.L. analyzed the bulk RNA-seq data; M.X. and Z.N. performed the flow cytometry experiments; M.X. performed the qRT-PCR experiments; M.X. and B.A.M. performed the RNAscope ISH experiments; M.X. and C.O. performed the IHC experiments; R.I. and G.D.B. provided the cell-cell interaction dataset; M.X., S.L.L., S.S.L., A.R., G.D.B. and J.Z.L. supervised aspects of the study; L.L.R. supervised the whole study; J.Z.L. and L.L.R. secured funding; M.X. wrote the original draft of the manuscript; S.L.L., S.M.B. and L.L.R. edited the manuscript; All authors reviewed the manuscript and approved its submission.

COMPETING FINANCIAL INTERESTS

The authors declare no competing interests.

FIGURE LEGENDS

Fig. 1. Identification of cell types. (A) Overview of the experimental workflow. (B) t-distributed stochastic neighbor embedding (t-SNE) projection of 37,069 cells derived from 8 young and 8 old mouse brains. Cell clusters were color-coded and annotated post hoc based on their transcriptional profile identities (see Supplementary Methods). (C) t-SNE visualization of 6 major cell populations showing the expression of representative well-known cell-type-specific marker genes. Numbers reflect the number of unique molecular identifiers (UMI) detected for the specified gene for each cell. (D) Violin plot showing the distribution of expression levels of known representative cell-type-enriched marker genes across all 25 cell types. Markers used: *Pdgfra*, OPC [29]; *Cldn11*, OLG [29]; *Npy*, OEG [36]; *Thbs4*, NSC [90-94]; *Cd44*, ARP [95]; *Gja1*, ASC [33]; *Cdk1*, NRP ; *Sox11*, ImmN [35]; *Syt1*, mNEUR [28]; *Baiap3*, NendC [96]; *Ccdc153*, EPC [30]; *Sspo*, HypEPC [39]; *Rax*, TNC [30]; *Ttr*, CPC [26]; *Cldn5*, EC [37]; *Kcnj8*, PC [37]; *Acta2*, VSMC [37]; *Alas2*, Hb-VC [34,97]; *Slc6a13*, VLMC [29,39]; *Slc47a1*, ABC [39]; *Tmem119*, MG [33]; *Plac8*, MNC [38]; *Pf4*, MAC [38]; *Cd209a*, DC [38,98]; *S100a9*, NEUT [38]. (E) Bar plot showing the total number of detected cells and the total number of detected genes per cell type.

Fig. 2. Aging-related population shifts and changes in gene expression. (A) Bar plot showing the fraction of cells associated with each cell type in both young and old brains (data presents mean ± SEM of 8 young and 8 old brains; *FDR<0.05 by Mann-Whitney *U* test). (B) Strip chart showing the aging-related logarithmic fold changes (logFC) of all detected genes across all cell types. Each point represents a gene. Genes in colored dots are significantly (FDR<0.05 and FC>10%) upregulated or downregulated with aging. Genes in gray are not significantly changed with aging. (C) Sample volcano plot for EC showing –log10(FDR) and logFC values for all genes with highlighting for those that are significantly upregulated (magenta dots) or downregulated (blue dots) with aging. Genes in black are not significantly changed with aging. (D) Heatmap of logFC showing a subset of aging-related genes (FDR<0.05 and FC>10%) that are shared across many of the major cell types. Gray indicates no significant dysregulation. (E) Heatmap of logFC showing a subset of aging-related genes (FDR<0.05 and FC>10%) that are unique to each major cell type.

Fig. 3. Validation of shared and cell-type-specific aging-related gene expression changes. (A) Violin plots with data in units of transcripts per million (TPM) from our scRNA-seq across all identified cell types (left panels) and RNAscope *in situ* hybridization images (middle panels) of mouse hippocampi showing the aging-related upregulation of

the ribosomal protein gene *Rpl6*, and of the lncRNAs *Malat1* and *Meg3*. This brain area was selected due to its high expression levels of those genes, according to the Allen Brain Atlas [99]. Scatter plots (right panels) showing the quantification of the RNAscope data of 3-4 independent experiments (data presents mean ± SEM; *p<0.05, **p<0.01 by Welch's t-test). Scale bar: 20μm. (B) Heatmap showing the fold expression changes (FC) of a few representative significantly (FDR<0.05) aging-related genes in MG, EC, and ASC as identified by our scRNA-seq (left panel) and verified by both bulk RNA-seq (middle panel) and qRT-PCR (right panel) on sorted CD11b$^+$ (MG), CD31$^+$ (EC) and ACSA-2$^+$ (ASC) cells. Gray indicates no aging-related gene expression changes in the seq data; consequently, these genes were not analyzed by qRT-PCR. For the qRT-PCR experiments data presents mean ± SEM of 3-9 young and 3-10 old mouse brains. (C) Scatter plots showing the significant correlations of the gene expression changes in (B) between the scRNA-seq, bulk RNA-seq and qRT-PCR datasets. Linear regression is depicted with the colored line, while black dotted lines represent 95% confidence intervals. Correlation coefficient (R^2) and p-value are shown at the bottom right of each plot. (D) Violin plots and immunohistochemistry showing the aging-related up-regulation of IL33 that is mainly expressed in OLG (see Supplementary Fig. 14), and the aging-related down-regulation of SPARC in MG (IBA1-positive cells; indicated by arrows). Scale bar: 50μm. Scatter plots showing the quantification of the immunohistochemistry data of 4 independent experiments (data presents mean ± SEM; *p<0.05 by Welch's t-test).

Fig. 4. Validation of bidirectional aging-related gene expression changes. (A-B) Violin plots with boxplots overlay of UMI from our scRNA-seq (left panels) and representative RNAscope *in situ* hybridization micrographs (middle panels) of mouse cortices showing the aging-related downregulation of *Cd9* in OPC (*Pdgfra*$^+$ cells; indicated by arrows) (A), and the aging-related upregulation of the same gene in MG (*Itgam*$^+$ cells; indicated by arrows) (B). Arrowheads in (B) designate autofluorescence from lipofuscin granules in the lysosomes of old microglia [100] (see details in Supplementary Methods). Violin plots with boxplots overlay (right panels) showing the quantification of the RNAscope experiments (data presents median expression of *Cd9* in *Pfgfra*$^+$ OPC and *Itgam*$^+$ MG derived from 4 young and 4 old brains; ****p<0.0001 by Mann-Whitney *U* test). Scale bar: 2μm. (C-D) Violin plots with boxplots overlay of UMI from our scRNA-seq (left panels) and representative RNAscope in *situ* hybridization micrographs (middle panels) of mouse cortices showing the aging-related downregulation of the ribosomal protein gene *Rps23* in OPC (C), and the aging-related upregulation of the same gene in MG (D). As in (B), arrowheads in (D) designate autofluorescence from lipofuscin granules. Dotted lines outline the area of each cell that was considered for quantification (see details in Supplementary Methods). Violin plots with boxplots overlay (right panels) showing the quantification of the RNAscope experiments (data presents median expression of *Rps23* in

Pfgfra$^+$ OPC and *Itgam*$^+$ MG derived from 4 young and 4 old brains; ****p<0.0001 by Mann-Whitney *U* test). Scale bar: 2μm.

Fig. 5. Aging-related changes in the expression of ribosomal protein genes. (A) Heatmap showing the logFC for all the significantly (FDR<0.05) aging-related ribosomal and translation-associated genes across 11 cell types, as identified by our scRNA-seq. Gray indicates no aging-related changes. (B) Heatmap of logFC showing all the significant (FDR<0.05) aging-related ribosomal protein genes and translation-associated genes across MG, EC and ASC as identified by our scRNA-seq (left panel) and further verified by bulk RNA-seq on sorted CD11b$^+$ (MG), CD31$^+$ (EC), and ACSA-2$^+$ (ASC) cells (right panel). The few inconsistencies presented here more probably reflect differences in the composition of the input sorted populations used for the comparisons (see details in Supplementary Methods). Of note, despite the fact that only a subset of these genes was found significantly dysregulated in our bulk RNA-seq analysis, due to lower statistical power, there is a significant correlation of the gene expression changes between the scRNA-seq and bulk RNA-seq datasets, as shown in scatter plot (C). More specifically, dots in (C) represent all genes from the examined cell types in (B). Linear regression is depicted with the colored line, while black dotted lines represent 95% confidence intervals. Correlation coefficient (R^2) and p-value are shown at the bottom right of the plot.

Fig. 6. Aging-related changes in cellular pathways and processes. Heatmap of gene set enrichment analysis (GSEA) showing a small subset of significant (p<0.05 and q<0.25) aging-related pathways across major cell types. Numbers in legend correspond to normalized enrichment scores (NES). Positive NES values indicate upregulation, while negative NES values indicate downregulation. Gray indicates no significant dysregulation with aging.

Fig. 7. Aging-related changes in intercellular communication. Panel (A) shows aging-related ligands produced and secreted by EC with receptors expressed in ASC, while panel (B) shows aging-related ligands produced and secreted by EC with receptors expressed in mNEUR. In both panels, nodes represent ligands or receptors expressed in the denoted cell type, and edges represent protein-protein interactions between them. Node color represents magnitude of differential gene expression (logFC as estimated by the MAST model), such that the most significantly age-upregulated genes are in magenta, and age-downregulated are in blue. Node borders indicate statistical significance of differential expression, specifically the false-discovery rate expected from the MAST analysis. Edge color represents the sum of scaled differential expression magnitudes from each

contributing node, while width and transparency are determined by the magnitude of scaled differential expression (see Supplementary Methods). These figures have been filtered such that the top 65 edges representing the most differentially expressed node pairs are shown. Figures for these cell interactions, and all others, are available from our interactive data viewer accessible at: https://baderlab.github.io/AgingMouseBrainCCInx/.

REFERENCES

1 Lopez-Otin, C., Blasco, M. A., Partridge, L., Serrano, M. & Kroemer, G. The hallmarks of aging. *Cell* **153**, 1194-1217, doi:10.1016/j.cell.2013.05.039 (2013).

2 Singh, P. P., Demmitt, B. A., Nath, R. D. & Brunet, A. The Genetics of Aging: A Vertebrate Perspective. *Cell* **177**, 200-220, doi:10.1016/j.cell.2019.02.038 (2019).

3 van Wijngaarden, P. & Franklin, R. J. Ageing stem and progenitor cells: implications for rejuvenation of the central nervous system. *Development* **140**, 2562-2575, doi:10.1242/dev.092262 (2013).

4 Wyss-Coray, T. Ageing, neurodegeneration and brain rejuvenation. *Nature* **539**, 180-186, doi:10.1038/nature20411 (2016).

5 Mattson, M. P. & Arumugam, T. V. Hallmarks of Brain Aging: Adaptive and Pathological Modification by Metabolic States. *Cell metabolism* **27**, 1176-1199, doi:10.1016/j.cmet.2018.05.011 (2018).

6 Lee, C. K., Weindruch, R. & Prolla, T. A. Gene-expression profile of the ageing brain in mice. *Nature genetics* **25**, 294-297, doi:10.1038/77046 (2000).

7 Zahn, J. M. *et al.* AGEMAP: a gene expression database for aging in mice. *PLoS genetics* **3**, e201, doi:10.1371/journal.pgen.0030201 (2007).

8 de Magalhaes, J. P., Curado, J. & Church, G. M. Meta-analysis of age-related gene expression profiles identifies common signatures of aging. *Bioinformatics* **25**, 875-881, doi:10.1093/bioinformatics/btp073 (2009).

9 Miller, J. A. *et al.* Neuropathological and transcriptomic characteristics of the aged brain. *eLife* **6**, doi:10.7554/eLife.31126 (2017).

10 Stilling, R. M. *et al.* De-regulation of gene expression and alternative splicing affects distinct cellular pathways in the aging hippocampus. *Frontiers in cellular neuroscience* **8**, 373, doi:10.3389/fncel.2014.00373 (2014).

11 Apostolopoulou, M. *et al.* Non-monotonic Changes in Progenitor Cell Behavior and Gene Expression during Aging of the Adult V-SVZ Neural Stem Cell Niche. *Stem cell reports* **9**, 1931-1947, doi:10.1016/j.stemcr.2017.10.005 (2017).

12 Dillman, A. A. *et al.* Transcriptomic profiling of the human brain reveals that altered synaptic gene expression is associated with chronological aging. *Scientific reports* **7**, 16890, doi:10.1038/s41598-017-17322-0 (2017).

13 Orre, M. *et al.* Acute isolation and transcriptome characterization of cortical astrocytes and microglia from young and aged mice. *Neurobiology of aging* **35**, 1-14, doi:10.1016/j.neurobiolaging.2013.07.008 (2014).

14 Grabert, K. *et al.* Microglial brain region-dependent diversity and selective regional sensitivities to aging. *Nature neuroscience* **19**, 504-516, doi:10.1038/nn.4222 (2016).

15 Galatro, T. F. *et al.* Transcriptomic analysis of purified human cortical microglia reveals age-associated changes. *Nature neuroscience* **20**, 1162-1171, doi:10.1038/nn.4597 (2017).
16 Boisvert, M. M., Erikson, G. A., Shokhirev, M. N. & Allen, N. J. The Aging Astrocyte Transcriptome from Multiple Regions of the Mouse Brain. *Cell reports* **22**, 269-285, doi:10.1016/j.celrep.2017.12.039 (2018).
17 Clarke, L. E. *et al.* Normal aging induces A1-like astrocyte reactivity. *Proceedings of the National Academy of Sciences of the United States of America* **115**, E1896-E1905, doi:10.1073/pnas.1800165115 (2018).
18 Olah, M. *et al.* A transcriptomic atlas of aged human microglia. *Nature communications* **9**, 539, doi:10.1038/s41467-018-02926-5 (2018).
19 Mrdjen, D. *et al.* High-Dimensional Single-Cell Mapping of Central Nervous System Immune Cells Reveals Distinct Myeloid Subsets in Health, Aging, and Disease. *Immunity* **48**, 380-395 e386, doi:10.1016/j.immuni.2018.01.011 (2018).
20 Hammond, T. R. *et al.* Single-Cell RNA Sequencing of Microglia throughout the Mouse Lifespan and in the Injured Brain Reveals Complex Cell-State Changes. *Immunity*, doi:10.1016/j.immuni.2018.11.004 (2018).
21 Kalamakis, G. *et al.* Quiescence Modulates Stem Cell Maintenance and Regenerative Capacity in the Aging Brain. *Cell* **176**, 1407-1419 e1414, doi:10.1016/j.cell.2019.01.040 (2019).
22 Spitzer, S. O. *et al.* Oligodendrocyte Progenitor Cells Become Regionally Diverse and Heterogeneous with Age. *Neuron* **101**, 459-471 e455, doi:10.1016/j.neuron.2018.12.020 (2019).
23 de Magalhaes, J. P. Programmatic features of aging originating in development: aging mechanisms beyond molecular damage? *FASEB journal : official publication of the Federation of American Societies for Experimental Biology* **26**, 4821-4826, doi:10.1096/fj.12-210872 (2012).
24 Xu, C. & Su, Z. Identification of cell types from single-cell transcriptomes using a novel clustering method. *Bioinformatics* **31**, 1974-1980, doi:10.1093/bioinformatics/btv088 (2015).
25 Levine, J. H. *et al.* Data-Driven Phenotypic Dissection of AML Reveals Progenitor-like Cells that Correlate with Prognosis. *Cell* **162**, 184-197, doi:10.1016/j.cell.2015.05.047 (2015).
26 Zeisel, A. *et al.* Brain structure. Cell types in the mouse cortex and hippocampus revealed by single-cell RNA-seq. *Science* **347**, 1138-1142, doi:10.1126/science.aaa1934 (2015).
27 Habib, N. *et al.* Div-Seq: Single-nucleus RNA-Seq reveals dynamics of rare adult newborn neurons. *Science* **353**, 925-928, doi:10.1126/science.aad7038 (2016).
28 Tasic, B. *et al.* Adult mouse cortical cell taxonomy revealed by single cell transcriptomics. *Nature neuroscience* **19**, 335-346, doi:10.1038/nn.4216 (2016).
29 Marques, S. *et al.* Oligodendrocyte heterogeneity in the mouse juvenile and adult central nervous system. *Science* **352**, 1326-1329, doi:10.1126/science.aaf6463 (2016).
30 Campbell, J. N. *et al.* A molecular census of arcuate hypothalamus and median eminence cell types. *Nature neuroscience* **20**, 484-496, doi:10.1038/nn.4495 (2017).

31 Habib, N. *et al.* Massively parallel single-nucleus RNA-seq with DroNc-seq. *Nature methods* **14**, 955-958, doi:10.1038/nmeth.4407 (2017).
32 Romanov, R. A. *et al.* Molecular interrogation of hypothalamic organization reveals distinct dopamine neuronal subtypes. *Nature neuroscience* **20**, 176-188, doi:10.1038/nn.4462 (2017).
33 Wu, Y. E., Pan, L., Zuo, Y., Li, X. & Hong, W. Detecting Activated Cell Populations Using Single-Cell RNA-Seq. *Neuron* **96**, 313-329 e316, doi:10.1016/j.neuron.2017.09.026 (2017).
34 Hrvatin, S. *et al.* Single-cell analysis of experience-dependent transcriptomic states in the mouse visual cortex. *Nature neuroscience* **21**, 120-129, doi:10.1038/s41593-017-0029-5 (2018).
35 Hochgerner, H., Zeisel, A., Lonnerberg, P. & Linnarsson, S. Conserved properties of dentate gyrus neurogenesis across postnatal development revealed by single-cell RNA sequencing. *Nature neuroscience* **21**, 290-299, doi:10.1038/s41593-017-0056-2 (2018).
36 Rosenberg, A. B. *et al.* Single-cell profiling of the developing mouse brain and spinal cord with split-pool barcoding. *Science* **360**, 176-182, doi:10.1126/science.aam8999 (2018).
37 Vanlandewijck, M. *et al.* A molecular atlas of cell types and zonation in the brain vasculature. *Nature* **554**, 475-480, doi:10.1038/nature25739 (2018).
38 Han, X. *et al.* Mapping the Mouse Cell Atlas by Microwell-Seq. *Cell* **172**, 1091-1107 e1017, doi:10.1016/j.cell.2018.02.001 (2018).
39 Zeisel, A. *et al.* Molecular Architecture of the Mouse Nervous System. *Cell* **174**, 999-1014 e1022, doi:10.1016/j.cell.2018.06.021 (2018).
40 Saunders, A. *et al.* Molecular Diversity and Specializations among the Cells of the Adult Mouse Brain. *Cell* **174**, 1015-1030 e1016, doi:10.1016/j.cell.2018.07.028 (2018).
41 Mickelsen, L. E. *et al.* Single-cell transcriptomic analysis of the lateral hypothalamic area reveals molecularly distinct populations of inhibitory and excitatory neurons. *Nature neuroscience* **22**, 642-656, doi:10.1038/s41593-019-0349-8 (2019).
42 Tepe, B. *et al.* Single-Cell RNA-Seq of Mouse Olfactory Bulb Reveals Cellular Heterogeneity and Activity-Dependent Molecular Census of Adult-Born Neurons. *Cell reports* **25**, 2689-2703 e2683, doi:10.1016/j.celrep.2018.11.034 (2018).
43 Bahar, R. *et al.* Increased cell-to-cell variation in gene expression in ageing mouse heart. *Nature* **441**, 1011-1014, doi:10.1038/nature04844 (2006).
44 Sim, F. J., Zhao, C., Penderis, J. & Franklin, R. J. The age-related decrease in CNS remyelination efficiency is attributable to an impairment of both oligodendrocyte progenitor recruitment and differentiation. *The Journal of neuroscience : the official journal of the Society for Neuroscience* **22**, 2451-2459, doi:20026217 (2002).
45 Artegiani, B. *et al.* A Single-Cell RNA Sequencing Study Reveals Cellular and Molecular Dynamics of the Hippocampal Neurogenic Niche. *Cell reports* **21**, 3271-3284, doi:10.1016/j.celrep.2017.11.050 (2017).
46 Walter, J., Keiner, S., Witte, O. W. & Redecker, C. Age-related effects on hippocampal precursor cell subpopulations and neurogenesis. *Neurobiology of aging* **32**, 1906-1914, doi:10.1016/j.neurobiolaging.2009.11.011 (2011).

47 Ben Abdallah, N. M., Slomianka, L., Vyssotski, A. L. & Lipp, H. P. Early age-related changes in adult hippocampal neurogenesis in C57 mice. *Neurobiology of aging* **31**, 151-161, doi:10.1016/j.neurobiolaging.2008.03.002 (2010).
48 Zahn, J. M. *et al.* Transcriptional profiling of aging in human muscle reveals a common aging signature. *PLoS genetics* **2**, e115, doi:10.1371/journal.pgen.0020115.eor (2006).
49 Subramanian, A. *et al.* Gene set enrichment analysis: a knowledge-based approach for interpreting genome-wide expression profiles. *Proceedings of the National Academy of Sciences of the United States of America* **102**, 15545-15550, doi:10.1073/pnas.0506580102 (2005).
50 Baruch, K. *et al.* Aging. Aging-induced type I interferon response at the choroid plexus negatively affects brain function. *Science* **346**, 89-93, doi:10.1126/science.1252945 (2014).
51 Stumm, R. K. *et al.* A dual role for the SDF-1/CXCR4 chemokine receptor system in adult brain: isoform-selective regulation of SDF-1 expression modulates CXCR4-dependent neuronal plasticity and cerebral leukocyte recruitment after focal ischemia. *The Journal of neuroscience : the official journal of the Society for Neuroscience* **22**, 5865-5878, doi:20026609 (2002).
52 Mi, W. *et al.* Cystatin C inhibits amyloid-beta deposition in Alzheimer's disease mouse models. *Nature genetics* **39**, 1440-1442, doi:10.1038/ng.2007.29 (2007).
53 Pitt, L. A. *et al.* CXCL12-Producing Vascular Endothelial Niches Control Acute T Cell Leukemia Maintenance. *Cancer cell* **27**, 755-768, doi:10.1016/j.ccell.2015.05.002 (2015).
54 Zou, J. *et al.* Cystatin C as a potential therapeutic mediator against Parkinson's disease via VEGF-induced angiogenesis and enhanced neuronal autophagy in neurovascular units. *Cell death & disease* **8**, e2854, doi:10.1038/cddis.2017.240 (2017).
55 Freeman, S. H. *et al.* Preservation of neuronal number despite age-related cortical brain atrophy in elderly subjects without Alzheimer disease. *Journal of neuropathology and experimental neurology* **67**, 1205-1212, doi:10.1097/NEN.0b013e31818fc72f (2008).
56 Rapp, P. R. & Gallagher, M. Preserved neuron number in the hippocampus of aged rats with spatial learning deficits. *Proceedings of the National Academy of Sciences of the United States of America* **93**, 9926-9930 (1996).
57 Rasmussen, T., Schliemann, T., Sorensen, J. C., Zimmer, J. & West, M. J. Memory impaired aged rats: no loss of principal hippocampal and subicular neurons. *Neurobiology of aging* **17**, 143-147 (1996).
58 Pilegaard, K. & Ladefoged, O. Total number of astrocytes in the molecular layer of the dentate gyrus of rats at different ages. *Analytical and quantitative cytology and histology* **18**, 279-285 (1996).
59 Tripathi, R. B. *et al.* Remarkable Stability of Myelinating Oligodendrocytes in Mice. *Cell reports* **21**, 316-323, doi:10.1016/j.celrep.2017.09.050 (2017).
60 Warren, L. A. *et al.* Transcriptional instability is not a universal attribute of aging. *Aging cell* **6**, 775-782, doi:10.1111/j.1474-9726.2007.00337.x (2007).

61 Martinez-Jimenez, C. P. *et al.* Aging increases cell-to-cell transcriptional variability upon immune stimulation. *Science* **355**, 1433-1436, doi:10.1126/science.aah4115 (2017).
62 Gonskikh, Y. & Polacek, N. Alterations of the translation apparatus during aging and stress response. *Mechanisms of ageing and development* **168**, 30-36, doi:10.1016/j.mad.2017.04.003 (2017).
63 Frenk, S. & Houseley, J. Gene expression hallmarks of cellular ageing. *Biogerontology*, doi:10.1007/s10522-018-9750-z (2018).
64 Makrides, S. C. Protein synthesis and degradation during aging and senescence. *Biological reviews of the Cambridge Philosophical Society* **58**, 343-422 (1983).
65 Lesur, I. & Campbell, J. L. The transcriptome of prematurely aging yeast cells is similar to that of telomerase-deficient cells. *Molecular biology of the cell* **15**, 1297-1312, doi:10.1091/mbc.e03-10-0742 (2004).
66 Yiu, G. *et al.* Pathways change in expression during replicative aging in Saccharomyces cerevisiae. *The journals of gerontology. Series A, Biological sciences and medical sciences* **63**, 21-34 (2008).
67 Sun, D. *et al.* Epigenomic profiling of young and aged HSCs reveals concerted changes during aging that reinforce self-renewal. *Cell stem cell* **14**, 673-688, doi:10.1016/j.stem.2014.03.002 (2014).
68 Kowalczyk, M. S. *et al.* Single-cell RNA-seq reveals changes in cell cycle and differentiation programs upon aging of hematopoietic stem cells. *Genome research* **25**, 1860-1872, doi:10.1101/gr.192237.115 (2015).
69 Carlson, K. A. *et al.* Genome-Wide Gene Expression in relation to Age in Large Laboratory Cohorts of Drosophila melanogaster. *Genet Res Int* **2015**, 835624, doi:10.1155/2015/835624 (2015).
70 Peters, M. J. *et al.* The transcriptional landscape of age in human peripheral blood. *Nature communications* **6**, 8570, doi:10.1038/ncomms9570 (2015).
71 Enge, M. *et al.* Single-Cell Analysis of Human Pancreas Reveals Transcriptional Signatures of Aging and Somatic Mutation Patterns. *Cell* **171**, 321-330 e314, doi:10.1016/j.cell.2017.09.004 (2017).
72 Davie, K. *et al.* A Single-Cell Transcriptome Atlas of the Aging Drosophila Brain. *Cell*, doi:10.1016/j.cell.2018.05.057 (2018).
73 Angelidis, I. *et al.* An atlas of the aging lung mapped by single cell transcriptomics and deep tissue proteomics. *Nature communications* **10**, 963, doi:10.1038/s41467-019-08831-9 (2019).
74 Sacramento, E. K. *et al.* Reduced proteasome activity in the aging brain results in ribosome stoichiometry loss and aggregation. *bioRxiv*, 577478 (2019).
75 Leeman, D. S. *et al.* Lysosome activation clears aggregates and enhances quiescent neural stem cell activation during aging. *Science* **359**, 1277-1283, doi:10.1126/science.aag3048 (2018).
76 Holtman, I. R. *et al.* Induction of a common microglia gene expression signature by aging and neurodegenerative conditions: a co-expression meta-analysis. *Acta neuropathologica communications* **3**, 31, doi:10.1186/s40478-015-0203-5 (2015).
77 Keren-Shaul, H. *et al.* A Unique Microglia Type Associated with Restricting Development of Alzheimer's Disease. *Cell* **169**, 1276-1290 e1217, doi:10.1016/j.cell.2017.05.018 (2017).

78 Mathys, H. *et al.* Temporal Tracking of Microglia Activation in Neurodegeneration at Single-Cell Resolution. *Cell reports* **21**, 366-380, doi:10.1016/j.celrep.2017.09.039 (2017).
79 Buchwalter, A. & Hetzer, M. W. Nucleolar expansion and elevated protein translation in premature aging. *Nature communications* **8**, 328, doi:10.1038/s41467-017-00322-z (2017).
80 Steffen, K. K. & Dillin, A. A Ribosomal Perspective on Proteostasis and Aging. *Cell metabolism* **23**, 1004-1012, doi:10.1016/j.cmet.2016.05.013 (2016).
81 Katsimpardi, L. *et al.* Vascular and neurogenic rejuvenation of the aging mouse brain by young systemic factors. *Science* **344**, 630-634, doi:10.1126/science.1251141 (2014).
82 Villeda, S. A. *et al.* Young blood reverses age-related impairments in cognitive function and synaptic plasticity in mice. *Nature medicine* **20**, 659-663, doi:10.1038/nm.3569 (2014).
83 Smith, L. K. *et al.* beta2-microglobulin is a systemic pro-aging factor that impairs cognitive function and neurogenesis. *Nature medicine* **21**, 932-937, doi:10.1038/nm.3898 (2015).
84 Castellano, J. M. *et al.* Human umbilical cord plasma proteins revitalize hippocampal function in aged mice. *Nature* **544**, 488-492, doi:10.1038/nature22067 (2017).
85 Chen, R., Wu, X., Jiang, L. & Zhang, Y. Single-Cell RNA-Seq Reveals Hypothalamic Cell Diversity. *Cell reports* **18**, 3227-3241, doi:10.1016/j.celrep.2017.03.004 (2017).
86 Grindberg, R. V. *et al.* RNA-sequencing from single nuclei. *Proceedings of the National Academy of Sciences of the United States of America* **110**, 19802-19807, doi:10.1073/pnas.1319700110 (2013).
87 Gupta, I. *et al.* Single-cell isoform RNA sequencing characterizes isoforms in thousands of cerebellar cells. *Nature biotechnology*, doi:10.1038/nbt.4259 (2018).
88 Soreq, L. *et al.* Major Shifts in Glial Regional Identity Are a Transcriptional Hallmark of Human Brain Aging. *Cell reports* **18**, 557-570, doi:10.1016/j.celrep.2016.12.011 (2017).
89 Rodriques, S. G. *et al.* Slide-seq: A scalable technology for measuring genome-wide expression at high spatial resolution. *Science* **363**, 1463-1467, doi:10.1126/science.aaw1219 (2019).
90 Beckervordersandforth, R. *et al.* In vivo fate mapping and expression analysis reveals molecular hallmarks of prospectively isolated adult neural stem cells. *Cell stem cell* **7**, 744-758, doi:10.1016/j.stem.2010.11.017 (2010).
91 Codega, P. *et al.* Prospective identification and purification of quiescent adult neural stem cells from their in vivo niche. *Neuron* **82**, 545-559, doi:10.1016/j.neuron.2014.02.039 (2014).
92 Llorens-Bobadilla, E. *et al.* Single-Cell Transcriptomics Reveals a Population of Dormant Neural Stem Cells that Become Activated upon Brain Injury. *Cell stem cell* **17**, 329-340, doi:10.1016/j.stem.2015.07.002 (2015).
93 Shah, P. T. *et al.* Single-Cell Transcriptomics and Fate Mapping of Ependymal Cells Reveals an Absence of Neural Stem Cell Function. *Cell* **173**, 1045-1057 e1049, doi:10.1016/j.cell.2018.03.063 (2018).
94 Zywitza, V., Misios, A., Bunatyan, L., Willnow, T. E. & Rajewsky, N. Single-Cell Transcriptomics Characterizes Cell Types in the Subventricular Zone and Uncovers

Molecular Defects Impairing Adult Neurogenesis. *Cell reports* **25**, 2457-2469 e2458, doi:10.1016/j.celrep.2018.11.003 (2018).

95 Liu, Y. *et al.* CD44 expression identifies astrocyte-restricted precursor cells. *Developmental biology* **276**, 31-46, doi:10.1016/j.ydbio.2004.08.018 (2004).

96 Zhang, X. *et al.* BAIAP3, a C2 domain-containing Munc13 protein, controls the fate of dense-core vesicles in neuroendocrine cells. *The Journal of cell biology* **216**, 2151-2166, doi:10.1083/jcb.201702099 (2017).

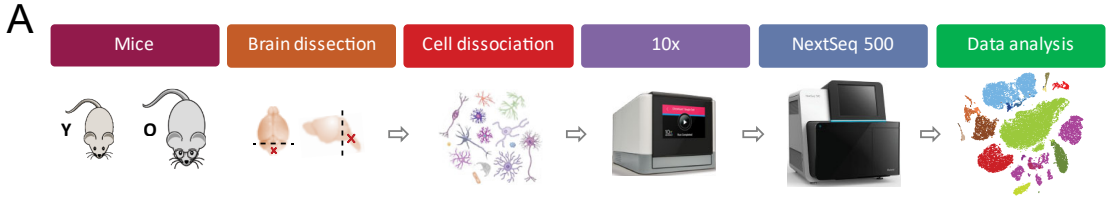
97 Straub, A. C. *et al.* Endothelial cell expression of haemoglobin alpha regulates nitric oxide signalling. *Nature* **491**, 473-477, doi:10.1038/nature11626 (2012).

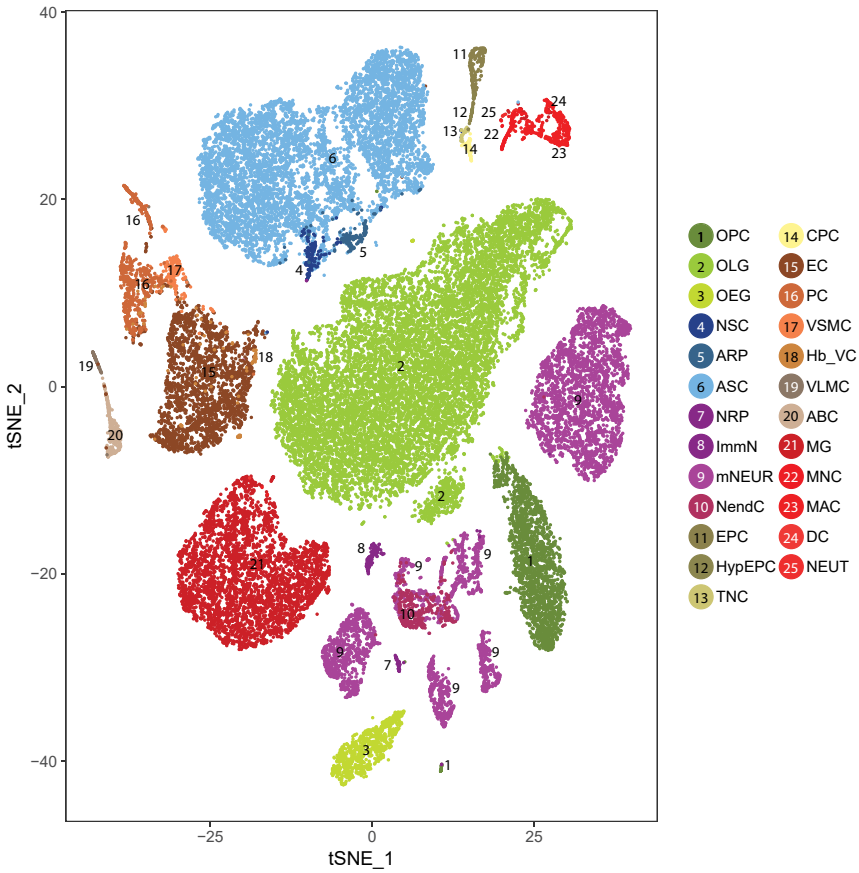
98 Geijtenbeek, T. B. *et al.* Identification of DC-SIGN, a novel dendritic cell-specific ICAM-3 receptor that supports primary immune responses. *Cell* **100**, 575-585 (2000).

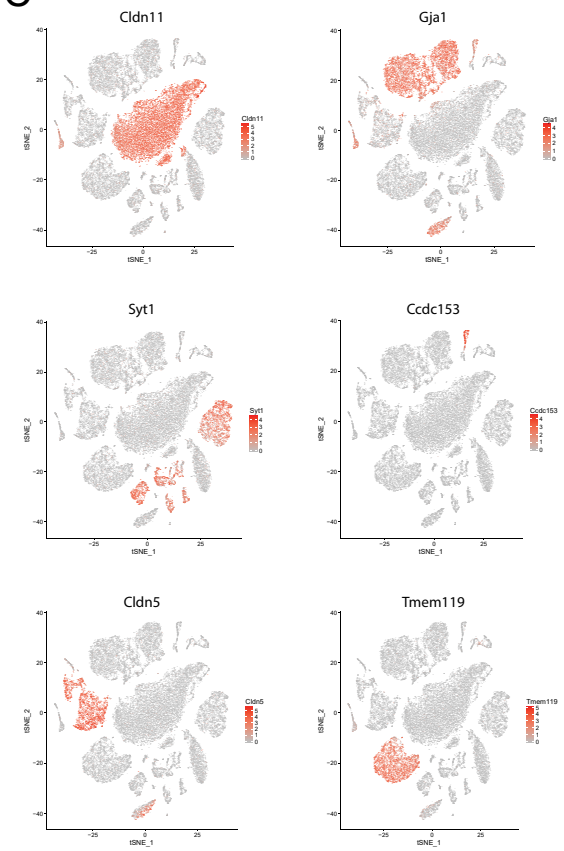
99 Lein, E. S. *et al.* Genome-wide atlas of gene expression in the adult mouse brain. *Nature* **445**, 168-176, doi:10.1038/nature05453 (2007).

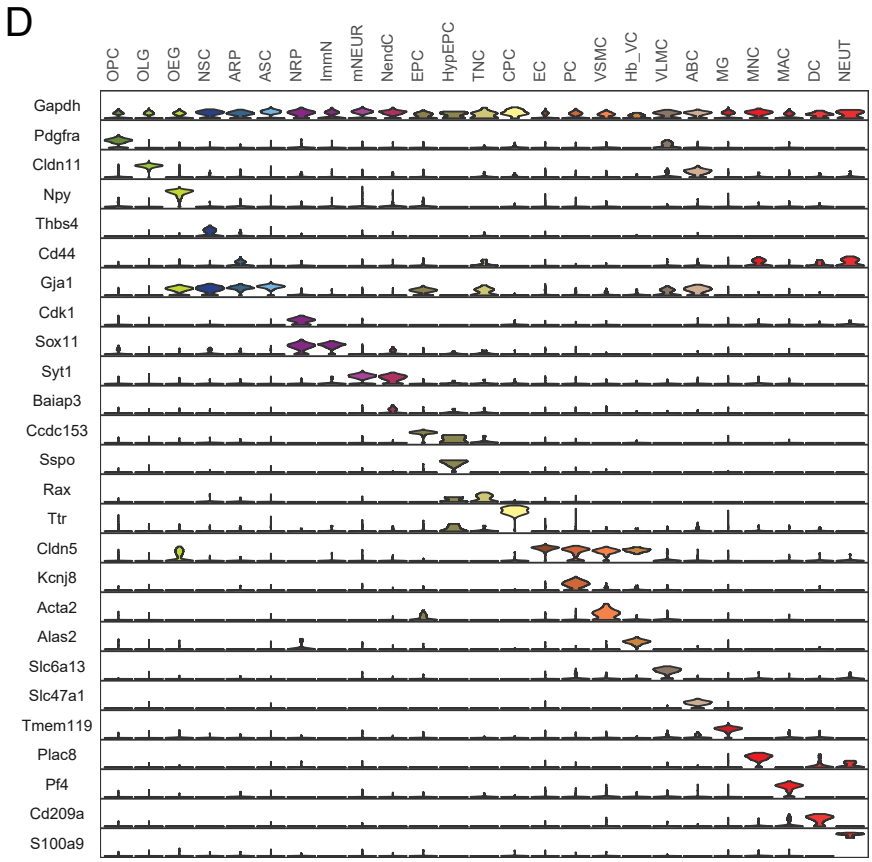
100 Xu, H., Chen, M., Manivannan, A., Lois, N. & Forrester, J. V. Age-dependent accumulation of lipofuscin in perivascular and subretinal microglia in experimental mice. *Aging cell* **7**, 58-68, doi:10.1111/j.1474-9726.2007.00351.x (2008).

Fig. 1


A
Mice
Brain dissection
Cell dissociation
10x
NextSeq 500
Data analysis
Y
O


B
tSNE_2
tSNE_1
1 OPC
2 OLG
3 OEG
4 NSC
5 ARP
6 ASC
7 NRP
8 ImmN
9 mNEUR
10 NendC
11 EPC
12 HypEPC
13 TNC
14 CPC
15 EC
16 PC
17 VSMC
18 Hb_VC
19 VLMC
20 ABC
21 MG
22 MNC
23 MAC
24 DC
25 NEUT


C
Cldn11
Gja1
Syt1
Ccdc153
Cldn5
Tmem119
tSNE_1
tSNE_2


D
OPC
OLG
OEG
NSC
ARP
ASC
NRP
ImmN
mNEUR
NendC
EPC
HypEPC
TNC
CPC
EC
PC
VSMC
Hb_VC
VLMC
ABC
MG
MNC
MAC
DC
NEUT
Gapdh
Pdgfra
Cldn11
Npy
Thbs4
Cd44
Gja1
Cdk1
Sox11
Syt1
Baiap3
Ccdc153
Sspo
Rax
Ttr
Cldn5
Kcnj8
Acta2
Alas2
Slc6a13
Slc47a1
Tmem119
Plac8
Pf4
Cd209a
S100a9

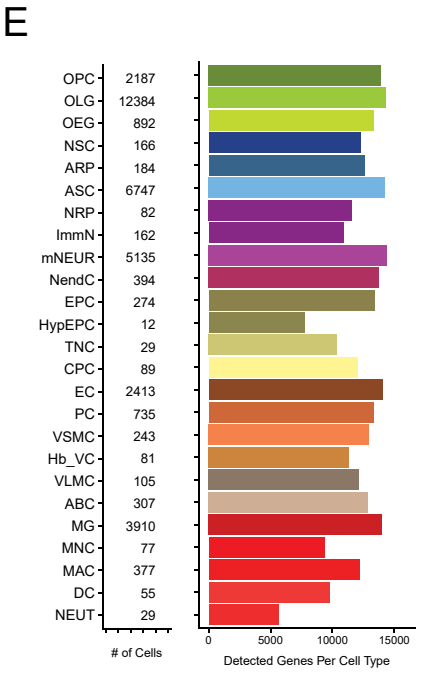
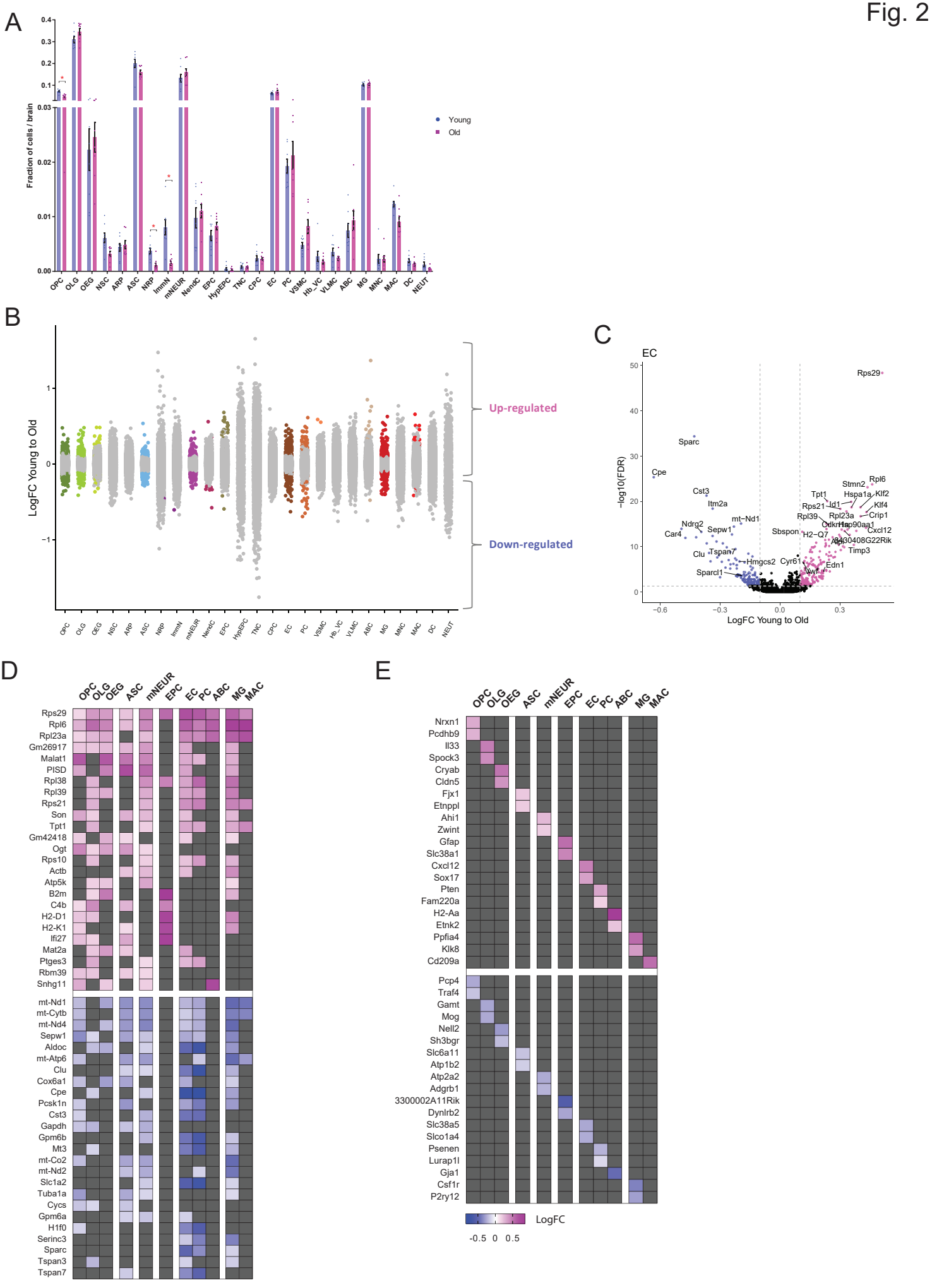
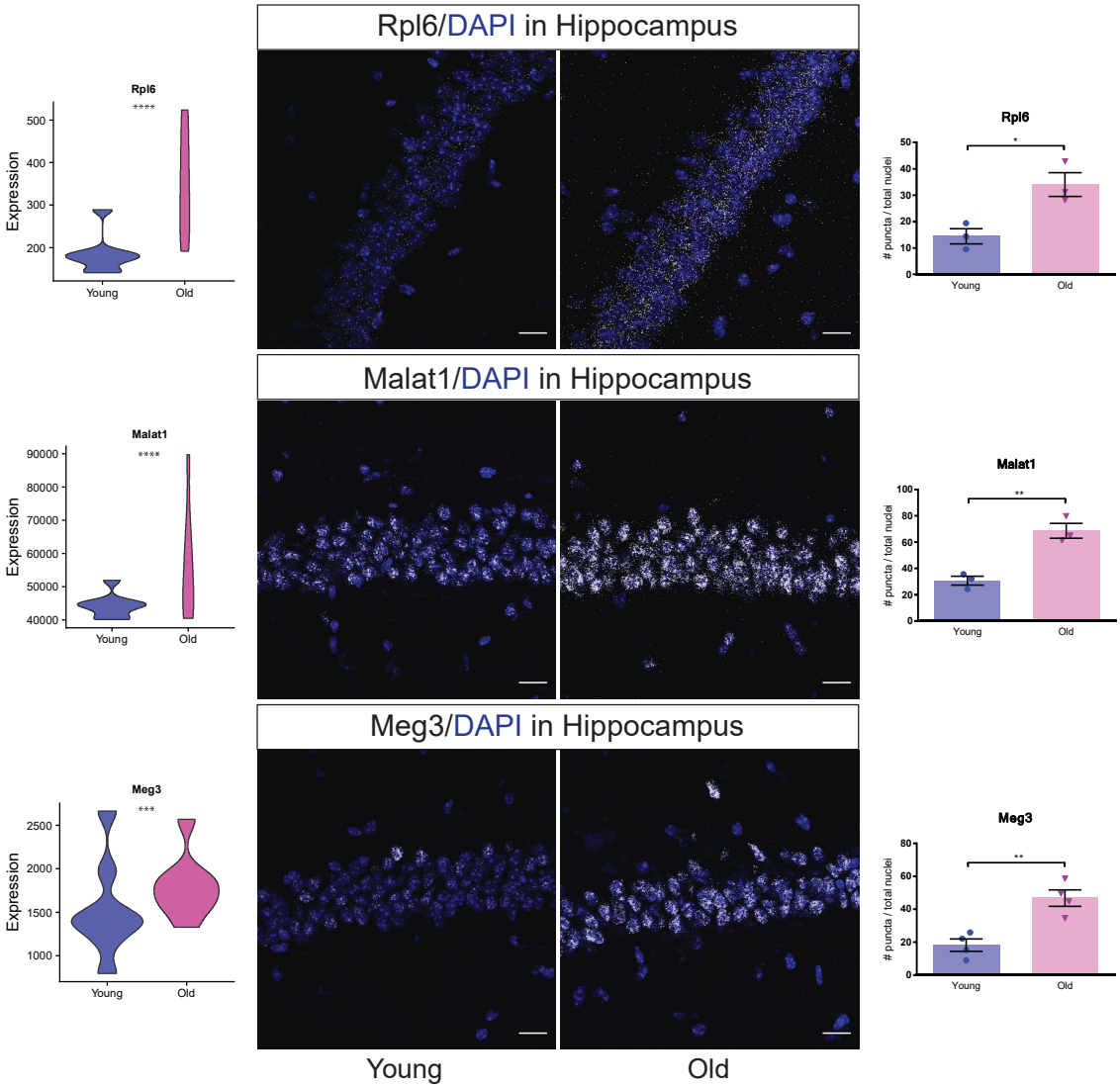

E
OPC 2187
OLG 12384
OEG 892
NSC 166
ARP 184
ASC 6747
NRP 82
ImmN 162
mNEUR 5135
NendC 394
EPC 274
HypEPC 12
TNC 29
CPC 89
EC 2413
PC 735
VSMC 243
Hb_VC 81
VLMC 105
ABC 307
MG 3910
MNC 77
MAC 377
DC 55
NEUT 29
# of Cells
0
5000
10000
15000
Detected Genes Per Cell Type

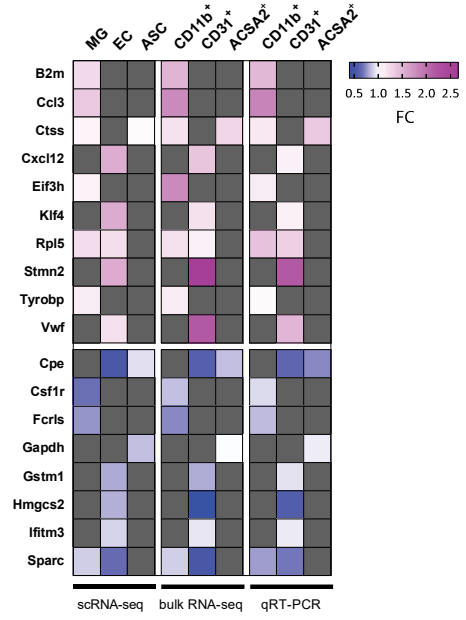
Fig. 2


A
Fraction of cells / brain
Young
Old
OPC OLG OEG NSC ARP ASC NRP ImmN mNEUR NendC EPC HypEPC TNC CPC EC PC VSMC Hb_VC VLMC ABC MG MNC MAC DC NEUT
B
LogFC Young to Old
Up-regulated
Down-regulated
C
EC
−log10(FDR)
LogFC Young to Old
Rps29
Sparc
Cpe
Cst3
Itm2a
mt-Nd1
Ndrg2
Car4
Sepw1
Clu
Tspan7
Sparcl1
Hmgcs2
Cyr61
Edn1
Sbspon
H2−Q7
Cxcl12
Timp3
Rpl6
Stmn2
Hspa1a
Klf2
Tpt1
Rps21
Id1
Klf4
Rpl39
Rpl23a
Crip1
Cdkn1a
Hsp90aa1
D
OPC OLG OEG ASC mNEUR EPC EC PC ABC MG MAC
Rps29 Rpl6 Rpl23a Gm26917 Malat1 PISD Rpl38 Rpl39 Rps21 Son Tpt1 Gm42418 Ogt Rps10 Actb Atp5k B2m C4b H2-D1 H2-K1 Ifi27 Mat2a Ptges3 Rbm39 Snhg11
mt-Nd1 mt-Cytb mt-Nd4 Sepw1 Aldoc mt-Atp6 Clu Cox6a1 Cpe Pcsk1n Cst3 Gapdh Gpm6b Mt3 mt-Co2 mt-Nd2 Slc1a2 Tuba1a Cycs Gpm6a H1f0 Serinc3 Sparc Tspan3 Tspan7
LogFC
-0.5 0 0.5
E
Nrxn1 Pcdhb9 Il33 Spock3 Cryab Cldn5 Fjx1 Etnppl Ahi1 Zwint Gfap Slc38a1 Cxcl12 Sox17 Pten Fam220a H2-Aa Etnk2 Ppfia4 Klk8 Cd209a
Pcp4 Traf4 Gamt Mog Nell2 Sh3bgr Slc6a11 Atp1b2 Atp2a2 Adgrb1 3300002A11Rik Dynlrb2 Slc38a5 Slco1a4 Psenen Lurap1l Gja1 Csf1r P2ry12
LogFC
-0.5 0 0.5

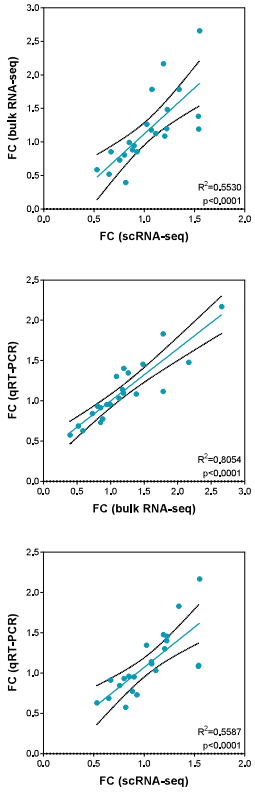
A


Rpl6/DAPI in Hippocampus
Malat1/DAPI in Hippocampus
Meg3/DAPI in Hippocampus
Rpl6
Malat1
Meg3
Expression
Young
Old
puncta / total nuclei

B


MG
EC
ASC
CD11b+
CD31+
ACSA2+
B2m
Ccl3
Ctss
Cxcl12
Eif3h
Klf4
Rpl5
Stmn2
Tyrobp
Vwf
Cpe
Csf1r
Fcrls
Gapdh
Gstm1
Hmgcs2
Ifitm3
Sparc
FC
scRNA-seq
bulk RNA-seq
qRT-PCR

C


FC (bulk RNA-seq)
FC (scRNA-seq)
R2=0,5530
p<0,0001
FC (qRT-PCR)
FC (bulk RNA-seq)
R2=0,8054
p<0,0001
FC (qRT-PCR)
FC (scRNA-seq)
R2=0,5587
p<0,0001

D

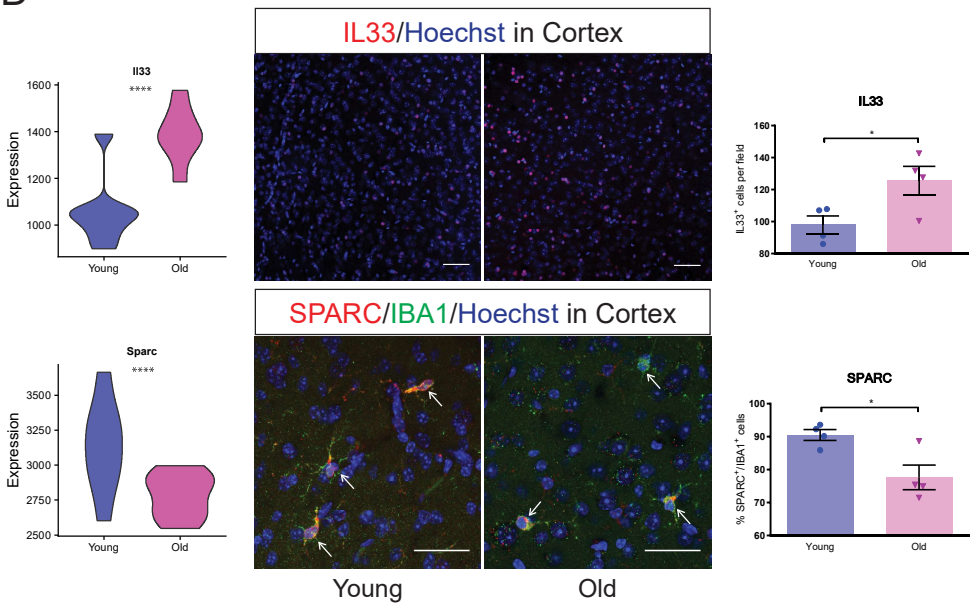

Il33
****
Expression
1600
1400
1200
1000
Young
Old
IL33/Hoechst in Cortex
IL33
*
IL33+ cells per field
160
140
120
100
80
Young
Old
Sparc
****
Expression
3500
3250
3000
2750
2500
Young
Old
SPARC/IBA1/Hoechst in Cortex
SPARC
*
% SPARC+/IBA1+ cells
100
90
80
70
60
Young
Old
Young
Old

Fig. 4

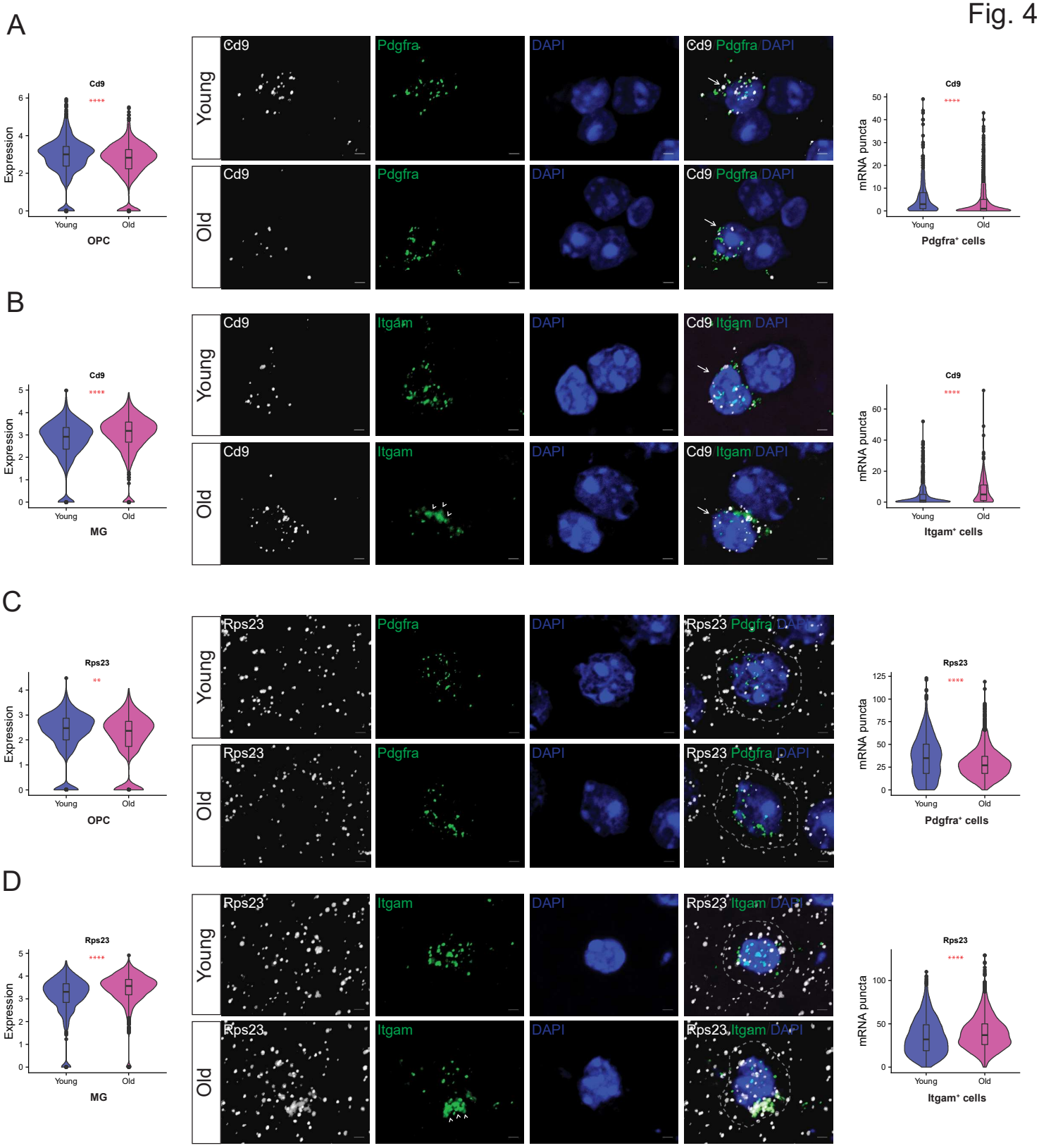

A
Cd9
Expression
Young
Old
OPC
Young
Old
Cd9
Pdgfra
DAPI
Cd9 Pdgfra DAPI
mRNA puncta
Pdgfra+ cells
B
MG
Itgam
Cd9 Itgam DAPI
Itgam+ cells
C
Rps23
OPC
Rps23 Pdgfra DAPI
D
MG
Rps23 Itgam DAPI

Fig. 5

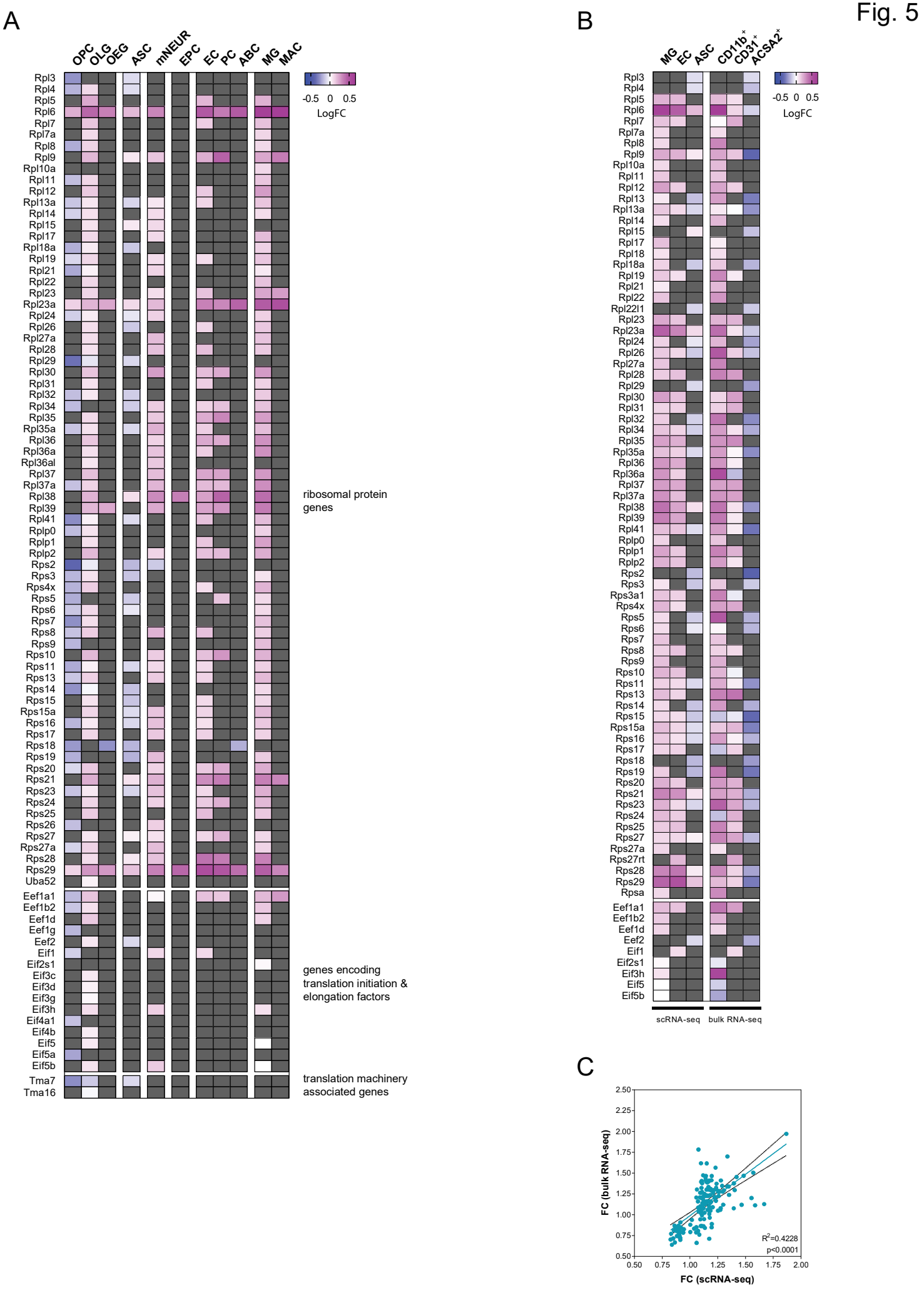
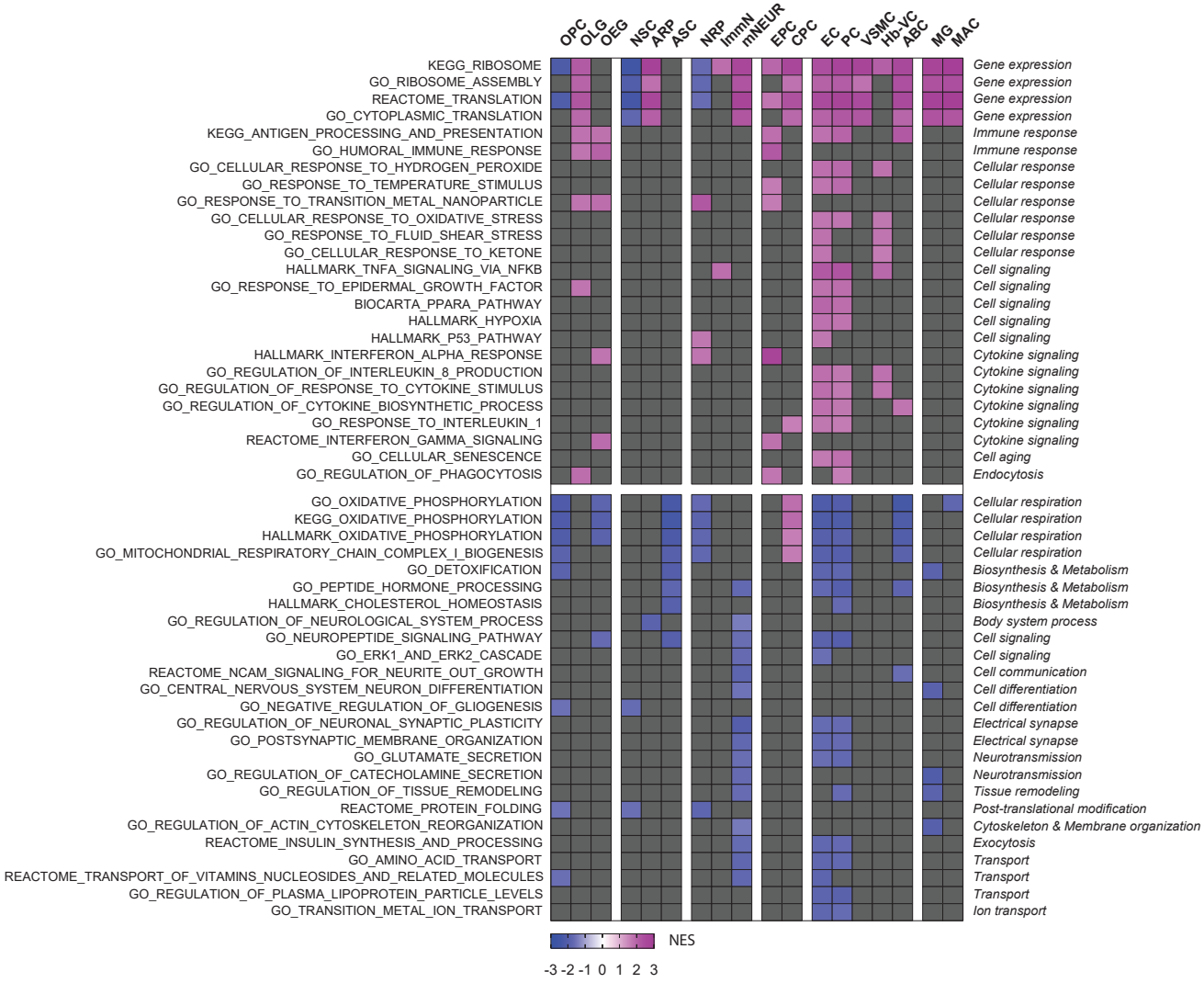
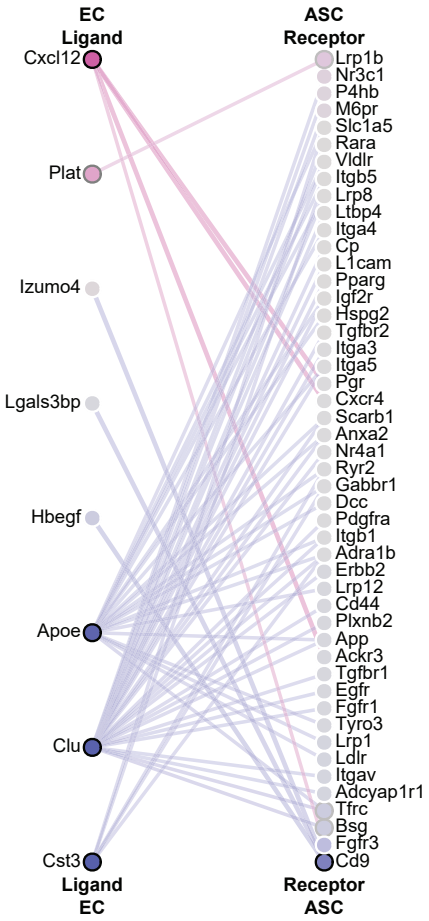

A
OPC
OLG
OEG
ASC
mNEUR
EPC
EC
PC
ABC
MG
MAC
-0.5 0 0.5
LogFC
ribosomal protein genes
genes encoding translation initiation & elongation factors
translation machinery associated genes
B
MG
EC
ASC
CD11b+
CD31+
ACSA2+
-0.5 0 0.5
LogFC
scRNA-seq
bulk RNA-seq
C
FC (bulk RNA-seq)
FC (scRNA-seq)
R2=0.4228
p<0.0001

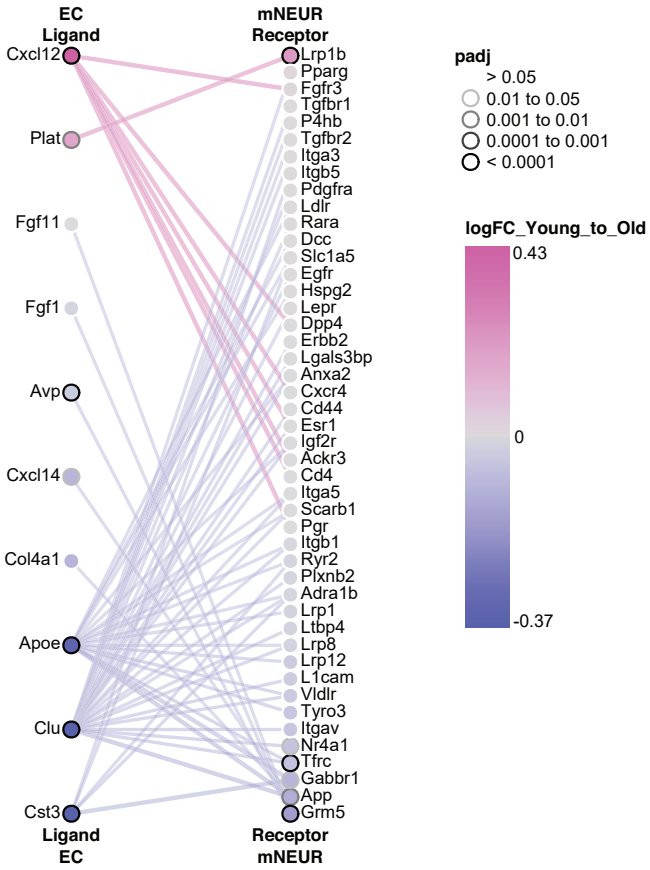
Fig. 6


OPC
OLG
OEG
NSC
ARP
ASC
NRP
ImmN
mNEUR
EPC
CPC
EC
PC
VSMC
Hb-VC
ABC
MG
MAC
KEGG_RIBOSOME
GO_RIBOSOME_ASSEMBLY
REACTOME_TRANSLATION
GO_CYTOPLASMIC_TRANSLATION
KEGG_ANTIGEN_PROCESSING_AND_PRESENTATION
GO_HUMORAL_IMMUNE_RESPONSE
GO_CELLULAR_RESPONSE_TO_HYDROGEN_PEROXIDE
GO_RESPONSE_TO_TEMPERATURE_STIMULUS
GO_RESPONSE_TO_TRANSITION_METAL_NANOPARTICLE
GO_CELLULAR_RESPONSE_TO_OXIDATIVE_STRESS
GO_RESPONSE_TO_FLUID_SHEAR_STRESS
GO_CELLULAR_RESPONSE_TO_KETONE
HALLMARK_TNFA_SIGNALING_VIA_NFKB
GO_RESPONSE_TO_EPIDERMAL_GROWTH_FACTOR
BIOCARTA_PPARA_PATHWAY
HALLMARK_HYPOXIA
HALLMARK_P53_PATHWAY
HALLMARK_INTERFERON_ALPHA_RESPONSE
GO_REGULATION_OF_INTERLEUKIN_8_PRODUCTION
GO_REGULATION_OF_RESPONSE_TO_CYTOKINE_STIMULUS
GO_REGULATION_OF_CYTOKINE_BIOSYNTHETIC_PROCESS
GO_RESPONSE_TO_INTERLEUKIN_1
REACTOME_INTERFERON_GAMMA_SIGNALING
GO_CELLULAR_SENESCENCE
GO_REGULATION_OF_PHAGOCYTOSIS
GO_OXIDATIVE_PHOSPHORYLATION
KEGG_OXIDATIVE_PHOSPHORYLATION
HALLMARK_OXIDATIVE_PHOSPHORYLATION
GO_MITOCHONDRIAL_RESPIRATORY_CHAIN_COMPLEX_I_BIOGENESIS
GO_DETOXIFICATION
GO_PEPTIDE_HORMONE_PROCESSING
HALLMARK_CHOLESTEROL_HOMEOSTASIS
GO_REGULATION_OF_NEUROLOGICAL_SYSTEM_PROCESS
GO_NEUROPEPTIDE_SIGNALING_PATHWAY
GO_ERK1_AND_ERK2_CASCADE
REACTOME_NCAM_SIGNALING_FOR_NEURITE_OUT_GROWTH
GO_CENTRAL_NERVOUS_SYSTEM_NEURON_DIFFERENTIATION
GO_NEGATIVE_REGULATION_OF_GLIOGENESIS
GO_REGULATION_OF_NEURONAL_SYNAPTIC_PLASTICITY
GO_POSTSYNAPTIC_MEMBRANE_ORGANIZATION
GO_GLUTAMATE_SECRETION
GO_REGULATION_OF_CATECHOLAMINE_SECRETION
GO_REGULATION_OF_TISSUE_REMODELING
REACTOME_PROTEIN_FOLDING
GO_REGULATION_OF_ACTIN_CYTOSKELETON_REORGANIZATION
REACTOME_INSULIN_SYNTHESIS_AND_PROCESSING
GO_AMINO_ACID_TRANSPORT
REACTOME_TRANSPORT_OF_VITAMINS_NUCLEOSIDES_AND_RELATED_MOLECULES
GO_REGULATION_OF_PLASMA_LIPOPROTEIN_PARTICLE_LEVELS
GO_TRANSITION_METAL_ION_TRANSPORT
Gene expression
Gene expression
Gene expression
Gene expression
Immune response
Immune response
Cellular response
Cellular response
Cellular response
Cellular response
Cellular response
Cellular response
Cellular response
Cell signaling
Cell signaling
Cell signaling
Cell signaling
Cell signaling
Cytokine signaling
Cytokine signaling
Cytokine signaling
Cytokine signaling
Cytokine signaling
Cytokine signaling
Cell aging
Endocytosis
Cellular respiration
Cellular respiration
Cellular respiration
Cellular respiration
Biosynthesis & Metabolism
Biosynthesis & Metabolism
Biosynthesis & Metabolism
Body system process
Cell signaling
Cell signaling
Cell communication
Cell differentiation
Cell differentiation
Electrical synapse
Electrical synapse
Neurotransmission
Neurotransmission
Tissue remodeling
Post-translational modification
Cytoskeleton & Membrane organization
Exocytosis
Transport
Transport
Transport
Ion transport
NES
-3 -2 -1 0 1 2 3

A


EC
Ligand
ASC
Receptor
Cxcl12
Plat
Izumo4
Lgals3bp
Hbegf
Apoe
Clu
Cst3
Lrp1b
Nr3c1
P4hb
M6pr
Slc1a5
Rara
Vldlr
Itgb5
Lrp8
Ltbp4
Itga4
Cp
L1cam
Pparg
Igf2r
Hspg2
Tgfbr2
Itga3
Itga5
Pgr
Cxcr4
Scarb1
Anxa2
Nr4a1
Ryr2
Gabbr1
Dcc
Pdgfra
Itgb1
Adra1b
Erbb2
Lrp12
Cd44
Plxnb2
App
Ackr3
Tgfbr1
Egfr
Fgfr1
Tyro3
Lrp1
Ldlr
Itgav
Adcyap1r1
Tfrc
Bsg
Fgfr3
Cd9
Ligand
EC
Receptor
ASC

B


EC
Ligand
mNEUR
Receptor
Cxcl12
Plat
Fgf11
Fgf1
Avp
Cxcl14
Col4a1
Apoe
Clu
Cst3
Lrp1b
Pparg
Fgfr3
Tgfbr1
P4hb
Tgfbr2
Itga3
Itgb5
Pdgfra
Ldlr
Rara
Dcc
Slc1a5
Egfr
Hspg2
Lepr
Dpp4
Erbb2
Lgals3bp
Anxa2
Cxcr4
Cd44
Esr1
Igf2r
Ackr3
Cd4
Itga5
Scarb1
Pgr
Itgb1
Ryr2
Plxnb2
Adra1b
Lrp1
Ltbp4
Lrp8
Lrp12
L1cam
Vldlr
Tyro3
Itgav
Nr4a1
Tfrc
Gabbr1
App
Grm5
Ligand
EC
Receptor
mNEUR
padj
> 0.05
0.01 to 0.05
0.001 to 0.01
0.0001 to 0.001
< 0.0001
logFC_Young_to_Old
0.43
0
-0.37

METHODS

Animals

C57BL/6J mice (JAX #000664) were housed in the Harvard Biolabs Animal Facility under standard conditions. All experimental procedures were approved in advance by the Animal Care and Use Committee of Harvard University (AEP #10-23) and are in compliance with federal and state laws. Young male mice were used at 2-3 months of age, and old male mice at 21-22 months of age.

Brain tissue dissociation

Here we modified existing dissociation protocols and developed a new protocol that enables the isolation of intact living cells from both young and old mouse brains in less than 1 hour. Briefly, mice were CO_2-anesthetized and then rapidly decapitated. Brains were extracted, and hindbrain regions were removed. The remaining brain tissue was dissociated into single cells using the Adult Brain Dissociation kit (Miltenyi Biotec #130-107-677) with these modifications: (a) the tissue was manually dissociated following the basic steps of the protocol described in the Neural Tissue Dissociation Kit (Miltenyi Biotec #130-092-628); (b) 5% (w/v) trehalose (Sigma Aldrich #T0167) was added in all buffers to ensure higher cellular viability [1]; (c) half concentration of papain was used, and the digestion was performed at 33-35^{o}C; (d) the enzymatic reaction was quenched using ovomucoid protease inhibitor, as described in the Papain Dissociation System (Worthington #LK003182); (e) cell clusters were removed by serial filtration through pre-wetted 70um (Falcon #352350) and 40um (Falcon #352340) nylon cell strainers; (f) myelin debris and erythrocyte removal steps were omitted to prevent any bias in the recovered cell yields; (g) all centrifugations were performed at 220xg for 8min at 4^{o}C. After dissociation, cells were kept on ice for no longer than 1 hour until further processing.

Single-cell RNA-sequencing

For the scRNA-seq experiments, 8 young and 8 old mouse brains were analyzed, with 2 animals sacrificed per day. Brain cells were processed through all steps to generate stable cDNA libraries. Briefly, after dissociation, cells were diluted in ice-cold PBS containing 0.4% BSA at a density of 1,000 cells/ul. For every sample, 17,400 cells were loaded into a Chromium Single Cell 3' Chip (10x Genomics) and processed following the manufacturer's instructions. Single-cell RNA-seq libraries were prepared using the Chromium Single Cell 3' Library & Gel Bead kit v2 and i7 Mutiplex kit (10X Genomics). Libraries were pooled based on their molar concentrations. Pooled libraries were then loaded at 2.07 pM and sequenced on a NextSeq 500 instrument (Illumina) with 26 bases for read1, 57 bases for read2 and 8 bases for Index1. Cell Ranger (version 1.2) (10X Genomics) was used to perform sample de-

multiplexing, barcode processing and single cell gene unique molecular identifier (UMI) counting, while a digital expression matrix was obtained for each experiment with default parameters [2], mapped to the 10X reference for mm10, version 1.2.0. After the initial sequencing, the samples in each pool were re-pooled based on the actual number of cells detected by Cell Ranger (Supplementary Fig. 2A), aiming to sequence each sample to a similar depth (number of reads/cell) (median: 40,007; Supplementary Fig. 2C). Multiple NextSeq runs were conducted to achieve over 70% sequencing saturation as determined again by Cell Ranger (median: 75%; Supplementary Fig. 2F).

Raw data processing and quality control for cell inclusion

Basic processing and visualization of the scRNA-seq data were performed using the Seurat package (version 2.3) in R (version 3.3.4) [3-5]. Our initial dataset contained 50,212 cells with data for 19,607 genes. The average numbers of UMI (nUMI) and non-zero genes (nGene) were 2876.70 and 1112.56 respectively. The data were log normalized and scaled to 10,000 transcripts per cell. Variable genes were identified with the FindVariableGenes() function with the following parameters used to set the minimum and maximum average expression and the minimum dispersion: x.low.cutoff = 0.0125, x.high.cutoff = 3, y.cutoff = 0.5. Next, principal component analysis (PCA) was carried out, and the top 20 principal components (PCs) were stored, which is the default number in Seurat. Clusters were identified with the FindClusters() function using the shared nearest neighbor (SNN) modularity optimization with a clustering resolution set to 1.6. All clusters with only one cell were removed. This method resulted in 40 initial clusters. Data for all cells are provided in Supplementary Fig. 3A with colors representing each of the clusters. For initial quality control filtering, we selectively removed entire clusters with the majority of cells having greater than 30% mitochondrial RNA, under 1,000 detected transcripts, or under 500 unique genes. Finally, we filtered the remaining individual cells using the following parameters: minimum percent mito = 0, maximum percent mito = 30%, minimum number of UMI = 250 maximum number of UMIs = 6000, minimum number of nGene = 250, and maximum number of nGene = 6000 to exclude outliers. Finally, we removed any genes that were only detected in fewer than 3 cells. After initial quality control (QC), we maintained a total of 38,244 cells and 14,699 genes. Data for all cells are provided in Supplementary Fig. 3B with black representing excluded cells and grey the included cells. The average nUMI, non-zero genes, percent mitochondrial RNA, and percent ribosomal RNA were 3199.12, 1284.08, 8.33%, and 6.94% respectively. PCA was again carried out, and the top 20 PCs were retained. The clustering was again performed with the clustering resolution now set to 2.0. This method resulted in 55 initial clusters. The final pre-processing stage was to remove likely doublet artifacts arising from the co-capture of multiple cells in one droplet. This step occurred following an initial round of determination of cell type identity as described in the next section. We first searched for the top differential markers for each

identified cluster/sub-cluster using the FindMarkers() function (Supplementary Table 3). Then, we defined doublets/multiplets as any cluster in which >30% of its cells express at least 5 of the top 10 genes specific for the initially identified cell type and any other cell type outside of the class of cell types it is associated with (see below for details on cell type classes). These clusters were removed from downstream analysis and clustering was again performed. Ultimately, we included 37,069 cells representing 38 clusters (Supplementary Fig. 4).

Determination of cell type identity

We used multiple cell-specific/enriched marker genes that have been previously described in the literature to assist in determining cell type identity (Fig. 1C-D). We then arranged all the identified cell types based on their expression profile, lineage, function and topology into 6 classes of cells (Supplementary Fig. 7A). For each group, we re-clustered the subcategorized cell types following the same strategy (top 20 PCs using a clustering resolution of 2.0). Only for the neuronal lineage, which has an increased complexity in terms of cell subtypes, we utilized the top 40 PCs to yield more separated clusters. The annotation of sub-clusters was performed similarly to identification of the main cell clusters.

Differential gene expression analysis

After initial quality control pre-processing and determination of cellular identities, we utilized the MAST package (version 1.6.1) [6] in R (version 3.3.4) to perform differential gene expression (DGE) analysis. Only cell types where at least half of the young and old animals had cells from that type were processed. For example, although we detected epithelial cells (*Epcam*$^{+}$/*Krt18*$^{+}$) in our dataset, we didn't process them as they were detected only in two of the young animals but none of the old animals. MAST generated p-values, fold changes (FC), and logFC (based on natural log of the fold changes) using a hurdle model with normalized nUMI as a covariate. It is worth mentioning that due to shrinkage in the Bayes approach leveraged by MAST, we were able to detect significance in very small changes in transcription but there was also an underestimation of fold change. This is especially noticeable when comparing fold change between MAST calculations and traditional TPM-based calculations for genes with low expression levels. Additionally, the DGE techniques employed here have more power to assign significance of subtle changes in highly transcribed genes and therefore our results may underrepresent changes in lowly transcribed genes. Finally, our ability to establish a baseline level of transcription is proportional to the number of cells measured and thus more subtle changes in abundant populations can be deemed significant.

Pathway analysis

Gene set enrichment analysis (GSEA) [7] was performed to identify cellular pathways and processes associated with aging. Analysis was carried out using the GSEA package (version 3.0) (Broad Institute), following the protocol described in Reimand et al. 2019 [8]. Briefly, prior to the analysis, genes for every distinct cell population were ranked according to their differential gene expression changes and significance (young vs. old). 2 pre-ranked gene lists were generated for each cell type: (1) with all genes transcribed, and (2) without the highly abundant mitochondrially-encoding genes and ribosomal protein genes. All of these pre-ranked gene lists were then used as an input, while 5 gene datasets [Hallmark pathways; GO biological processes; KEGG; BioCarta; Reactome (versions 6.1)] were used as a reference. One thousand random permutations were performed to calculate the p-values for each pathway. Only gene sets with $p<0.05$ and $q<0.25$ were considered as significantly enriched. To overcome redundancy and help interpretation of the analysis, we grouped terms over-representing the same pathway using the Cytoscape software (version 3.5.1) and the AutoAnnotate app (version 1.2) [9]. Pathways belonging to similar biological processes were also grouped together for easier navigation/exploration (Supplementary Table 7). Unless otherwise stated, expression heatmaps for specific pathways and processes were generated using the raw normalized expression (TPM) values. More specifically, for each value in a row of expression the mean of the row was subtracted followed by division by the row's standard deviation.

Intercellular network analysis

Cell-cell interactions were predicted by a method similar to that described by Kirouac et al. [10]. First, a cell communication interactome was created, collecting known protein-protein interactions between receptor, ligand, and extracellular matrix (ECM) proteins. Receptor genes were defined based on a set of GO terms (GO: 0043235 - receptor complex; GO: 0008305 - integrin complex; GO: 0072657 - protein localized to membrane; GO: 0043113 - receptor clustering; GO: 0004872 - receptor activity; GO: 0009897 - external side of plasma membrane) and UniProt (search term: "Receptor [KW-0675]" GO: 0005886 organism: human). Ligand genes were defined based on a GO term (GO: 0005102 - receptor binding) and the set of proteins labeled as secreted in the Secretome dataset (https://www.proteinatlas.org/humanproteome/secretome) [11]. ECM genes were defined based on a set of GO terms (GO: 0031012 - extracellular matrix; GO: 0005578 - proteinacious extracellular matrix; GO: 0005201 - extracellular matrix structural constituent; GO: 1990430 - extracellular matrix protein binding; and GO: 0035426 - extracellular matrix cell signalling). Gene lists were manually curated to correct or remove

genes that were misclassified. Using the curated list of receptors, ligands, and ECM genes, known protein-protein interactions were collected from iRefindex (version 14) [12], Pathway Commons (version 8) [13], and BioGRID (version 3.4.147) [14], keeping only those occurring between genes from the different classes (ligand, receptor, ECM). This dataset is available at: https://baderlab.org/CellCellInteractions. To predict cell-cell interactions, the ligand-receptor interaction dataset was filtered for genes detected to be expressed at the mRNA transcript level in our cell types. To investigate aging-related perturbations in these putative cell-cell interaction networks, differential gene expression metrics from the MAST analysis outlined above were used to build subnetworks for each set of interactions between cell types. In these networks, nodes represent ligands or receptors expressed in the denoted cell type, and edges represent protein-protein interactions between them. Nodes were colored to represent the magnitude of differential gene expression (logFC as estimated by the MAST model). These values were scaled per cell type and summed to determine edge weight. An R Shiny application was built to interactively explore the bipartite graphs generated from this analysis and is available at: https://baderlab.github.io/AgingMouseBrainCCInx/.

Flow cytometry

For the simultaneous isolation and purification of ASC, EC, and MG, we developed a multicolor flow cytometry approach. Briefly, dissociated cells from each brain were pelleted (220xg, 8min, 4^{o}C) and resuspended in 1ml ice-cold labeling buffer (HBSS without calcium and magnesium, 0.1% BSA, 2mM EDTA, 5% trehalose, 1% GlutaMAX). Cells were incubated with 100ul of FcR blocking reagent (Miltenyi Biotec #130-092-575) for 12min at 4^{o}C under continuous rotation, and then labeled with 3ug/ml of each of the following antibodies: APC anti-ACSA-2 (Miltenyi Biotec #130-102-315) for ASC; BV786 anti-CD31 (BD Biosciences #740870 and BD Biosciences #740879) for EC; and BV510 anti-CD11b (BD Biosciences #562950) for MG. Cells were also incubated with the following antibodies targeting unwanted cell populations: PE anti-CD200 (BioLegend #123808) for mNEUR and Alexa Fluor 488 anti-O4 (R&D Systems #FAB1326G) for OLG. This step is critical as it helps to exclude unwanted cells during sorting, thus minimizing cross-contamination events. After 12min of incubation at 4^{o}C (in dark conditions), cells were washed extensively, pelleted and resuspended in ice-cold FACS buffer (HBSS containing calcium and magnesium, 0.5% BSA, 5% trehalose, 1% Glutamax) in a volume of 25ml per brain (5 FACS tubes). To exclude cellular debris and dead cells, 15min before sorting, 10uM Calcein Blue AM (BD Biosciences #564060) was added to the FACS tubes to stain live cells. Calcein^{+} cells were then sorted using a Moflo Astrios instrument (Beckman Coulter) with a 70um nozzle at 60psi. Gates were set manually by using compensation beads (Life Technologies #A10497) and appropriate control samples, and data were analyzed with FlowJo software

(version 10). For the purification of EPC, we followed a similar flow cytometry approach using these antibodies: APC anti-CD133 (Miltenyi Biotec #130-102-197); APC anti-CD133 (eBioscience #17-1331-81); PE anti-CD24a (BD Biosciences #553262); and PE anti-CD24a (BioLegend #138504). To minimize RNA degradation, sorted cells were collected directly in RL buffer (Norgen Biotek #48500) supplemented with 10% BME, in a 1:1 final ratio (50% lysis buffer : 50% cells in sheath fluid; the PBS-based solution that is derived from the flow cytometer). After sorting, cell lysates were snap frozen and stored at -80^{o}C for up to 1 month until further processing.

RNA extraction

Total RNA was extracted from sorted cells using the total RNA purification plus Micro kit (Norgen Biotek #48500) following the manufacturer's instructions. Prior to RNA extraction, a chloroform extraction step was included to remove myelin debris/lipids, as well as, an on-column DNase digestion step (Qiagen #79254) to remove genomic and mitochondrial DNA. For all samples, RNA concentration was determined using a Qubit Fluorometer (Invitrogen), while RNA purity and integrity were evaluated with a BioAnalyzer instrument (Agilent). After extraction, RNA was immediately stored at -80^{o}C for no longer than a month until further processing.

Bulk RNA sequencing

For the bulk RNA-seq experiments, sorted/purified cells from 8 mouse brains (4 young and 4 old) were analyzed. Bulk RNA-seq was performed using a modified version of the SCRB-Seq that was originally developed for single cell RNA-seq analysis [15]. Briefly, polyadenylated RNA, from total RNA (7.5-25ng; RIN values >6.5) extracted from our FACS-purified cells, with ERCC Spike-in control Mix A (Ambion) at 10^{-6} final dilution, were converted to cDNA and decorated with universal adapters, sample-specific barcodes and UMI using a template-switching reverse transcriptase. Decorated cDNA was then pooled, amplified and prepared for multiplexed sequencing (NextSeq500, Illumina) using a modified transposon-based fragmentation approach that enriched for 3' ends and preserved strand information.

Bulk sequencing data analysis

Post-sequencing quality control on each of the libraries was performed to assess coverage depth, enrichment for messenger RNA (exon/intron and exon/intergenic density ratios), fraction of rRNA reads and number of detected genes using bespoke scripts. Second

sequence reads were aligned against the murine genome mm9 using bwa mem (version 0.7.10-r789) (http://bio-bwa.sourceforge.net/). Gene expression was estimated based on reads mapping near the 3' end of transcripts using ESAT [16], based on the mm9 Refseq annotation, with flags java -Xmx128G -task score3p -wLen 50 -wExt 5000 -wOlap 0 -sigTest 0.01 -multimap ignore. Results were summarized as counts per million mapped reads (CPM), merged across samples, log-transformed and subjected to hierarchical clustering and visualization. For ERCC quantification, reads were mapped against the ERCC sequences using STAR (version 2.5.1b) [17] with flags --runMode alignReads --runThreadN 8 –outSAMtype BAM SortedByCoordinate –outFilterType BySJout --outFilterMultimapNmax 20 --outFilterMismatchNmax 999 --alignIntronMin 10 –alignIntronMax 1000000 --alignMatesGapMax 1000000 --alignSJoverhangMin 8 --alignSJDBoverhangMin 1 --quantMode TranscriptomeSAM. Bam files from STAR were sorted and indexed with samtools [18] and counts were retrieved from the indices using idxstats. Differential gene expression (DGE) analysis [19] was performed in R (version 3.2.3) using Bioconductor's DESeq2 package (version 3.7) [20]. Dataset parameters were estimated using the estimateSizeFactors(), and estimateDispersions() functions; read counts across conditions were modeled based on a negative binomial distribution and a Wald test was used to test for differential expression (nbinomWaldtest(), all packaged into the DESeq() function), using the age as a contrast.

Quantitative Real time PCR

For the quantitative Real-Time PCR (qRT-PCR) experiments, sorted/purified cells from 19 mouse brains (9 young and 10 old) were analyzed. Briefly, RNA samples with RIN values >6.5 were reverse transcribed into cDNA using the iScript cDNA synthesis kit (Bio-Rad #170-8891) following the manufacturer's instructions. The resulting cDNA was then processed for qRT-PCR analysis using pre-designed primers (Integrated DNA Technologies) (Supplementary Table 9) and the Fast SYBR Green Master Mix (Life Technologies #4385614) in a QuantStudio 12K Flex Real-Time PCR System (Applied Biosystems). Before data analysis, we examined the melting curves for each reaction and included only those with a single peak at the expected melting temperature. The fold-change (FC) in gene expression was determined by the $2^{-\Delta\Delta C_T}$ method [21], and all values were normalized to the endogenous expression of *Vcp*; a housekeeping gene that has been proposed for calibration in quantitative experiments [22]. Our scRNA-seq analysis showed that in the vast majority of cell populations *Vcp* levels remain unaltered with aging, in contrast to other more commonly used genes. Samples with *Vcp* Ct values >29 were excluded from our analysis. Each sample was repeated in technical duplicates on 3-10 biological replicates.

Comparison of gene expression changes across different datasets

Unless stated otherwise, heatmaps of LogFC were used for the comparison of gene expression changes across different datasets (scRNA-seq, FACS/bulk RNA-seq, FACS/qRT-PCR). Heatmaps are much more informative compared to Venn diagrams as they display gene identity and the degree of expression change. Our independent datasets were in a very good agreement with each other, as only a few inconsistencies in the expression changes of certain individual genes were observed. These changes more likely reflect slight differences in the cell populations identified either informatically (for scRNA-seq) or by antibody labeling (for FACS/bulk RNA-seq). For example, in our flow cytometry experiments we used anti-ACSA-2 to isolate and purify astrocytes [23,24], but a recent study showed that this marker is not expressed at the same level by all astrocytes [25]. Thus, this marker may slightly enrich some subpopulations of astrocytes more than others. Of note, the existence of diverse subpopulations of astrocytes with distinct regional-specific transcriptomic signatures has been recently demonstrated [26], and verified by our scRNA-seq analysis (see Supplementary Fig. 8), while aging-associated gene expression changes in different regional astrocytes have been also documented [27-29]. Therefore, it is possible that informatics-based identification, and FACS-based isolation/purification, define cell populations that are very similar, but not identical, to each other, potentially contributing to discrepancies when comparative analyses are employed.

RNAscope *In Situ* Hybridization

RNAscope fluorescent *in situ* hybridization was performed on fresh-frozen brain tissue from 16 mice (8 young and 8 old). For sample preparation, mice were CO_2-anesthetized, and brains were rapidly extracted and embedded in OCT (Tissue Tek) on dry ice, and then stored at -80°C until further processing. We collected 14µm cryostat sections and RNAscope hybridizations were carried out according to the manufacturer's instructions, using the RNAscope Multiplex Fluorescent Manual Assay kit (Advanced Cell Diagnostics). Briefly, thawed sections were dehydrated in sequential incubations with ethanol, followed by 30 min Protease IV treatment and washing in 1x PBS. Appropriate combinations of hybridization probes were incubated for 2 hours at 40°C, followed by four amplification steps, DAPI counterstaining, and mounting with Prolong Gold mounting medium (Thermo Fisher Scientific #P36930). For single probe analysis, probes against *Rpl6* (ACD #300031), *Malat1* (ACD #313391), and *Meg3* (ACD #527201) were tested and labeled using the fluorophore Atto-550nm. For each mouse, 3-4 bregma-matched sections were imaged. Images (4 per brain section) were acquired using a Zeiss LSM 880 Confocal Microscope using identical settings across young and old sections and represented as maximum intensity projections of acquired confocal z stacks. Analysis was done using the CellProfiler software (version 3) [30] with the following specifications for different target probes:

Malat1/Meg3: only puncta with a diameter between 4-8 pixels that were located within the nuclei were quantified; *Rpl6*: only puncta with a diameter between 4-8 pixels that were located within the perinuclear space (within 70 pixels of the DAPI-positive nuclei) were quantified. For dual probe analysis, RNAscope was performed as described above, but here imaging settings were kept identical across all young and old brain sections and all probes tested. Probes against *Cd9* (ACD #430631), *Rps23* (ACD #571741), *Pdgfra* (ACD #480661-C3), and *Itgam* (ACD #311491-C3) were tested. Target probes (*Cd9*, *Rps23*) were labeled by fluorophore Atto-550nm while cell type markers (*Pdgfra*, *Itgam*) were labeled by fluorophore Alexa-488nm. An empty channel (Atto-647) was collected for every image processed to account for autofluorescence from lipofuscin granules largely associated in the aged brain with microglia [31]. In our imaging we observed that lipofuscin autofluorescence mainly interfered with Alexa-488 channel. Imaging analysis was performed as above with the following specifications for target probes (*Cd9, Rps23*): only puncta with a diameter between 6-15 pixels that were located within an OPC's or MG's perinuclear space (within 70 pixels of the DAPI-positive nuclei) were quantified. OPC and MG were defined as cells that contained at least two *Pdgfra*$^+$ or *Itgam*$^+$ puncta respectively (diameter 6-15 pixels). It is important to note that due to the high degree of homology among ribosomal protein genes, certain pseudogenes and predicted mouse genes, probes designed against *Rpl6* and *Rps23* may also cross-detect off-targets, based on the specificity criteria provided by the vendor: *Rpl6* probe may cross-detect: *Gm13397*, *Gm6807*; *Rps23* probe may cross-detect *Gm8624*, *Gm3189*, *Gm10689*, *Rps23-ps1*, *Rps23-ps2*.

Immunohistochemistry

For immunohistochemistry experiments, 14 mouse brains (7 young and 7 old) were processed. For preparation of free-floating tissue sections, mice were perfused intracardially with 1x PBS followed by 4% paraformaldehyde (PFA), brains were removed and embedded in 3% agarose, and serial 30µm-thick coronal sections were cut in a vibrating microtome and were kept in 1x PBS with 0.1% sodium azide at 4°C until staining. For preparation of fresh-frozen tissue sections (used only to show the co-expression of IL33 and OLIG2), mice were CO_2-anesthetized, brains were rapidly extracted and embedded in OCT, and serial 14µm-thick coronal sections were cut in a cryostat and then fixed in 4% PFA prior to staining. Immunostaining was performed using standard procedures. Briefly, sections were washed thoroughly in 1x PBS and incubated in a permeabilization/blocking solution [10% normal goat serum (or 10% donkey serum, or 2% horse serum), 0.25% Triton X-100, 1x PBS] for 1 hour at room temperature. Sections were then incubated overnight at 4°C with the following primary antibodies in blocking solution: goat polyclonal anti-SPARC (R&D Systems #AF942), rabbit polyclonal anti-IBA1 (Wako #019-19741), goat polyclonal anti-IL33 (R&D Systems #AF3626), and mouse

monoclonal anti-OLIG2 (Millipore #MABN50). Alexa Fluor secondary antibodies (Invitrogen) were used for detection of primary antibodies in 1% normal goat (or donkey serum or horse serum), 1x PBS for 1-2 hours at room temperature. Hoechst 33342 was used to label nuclei. Imaging was performed using a Zeiss ELYRA super-resolution confocal microscope (free-floating tissue sections) or a Zeiss LSM 880 confocal microscope (fresh-frozen tissue sections) at 20x and 40x magnifications. Images were visualized using Zeiss Zen software (blue edition; version 2.6). For each mouse, 3-4 bregma-matched sections were imaged. Images were represented as maximum intensity projections of acquired confocal z-stacks. Analysis was done using Image J software (version 1.49).

Statistical analysis

All statistical analyses were performed using R (version 3.3.4) or GraphPad Prism (version 7.04). Unless otherwise stated, to generate p-values for cell counts and other metrics/variables (nGene, nUMI, CV) we used the Mann-Whitney *U* test [32]. All p-values modified to a false discovery rate (FDR) of 5% using the Benjamin-Hochberg precedure [33].

Data availability

The raw sequencing data are available through NCBI's Gene Expression Omnibus (GEO) under the accession number GSE129788. To further facilitate the exploration and utilization of our scRNA-seq data, readers can view and download the processed datasets through the Broad's Single Cell Data Portal:

https://portals.broadinstitute.org/single_cell/study/aging-mouse-brain

References:

1 Saxena, A. *et al.* Trehalose-enhanced isolation of neuronal sub-types from adult mouse brain. *BioTechniques* **52**, 381-385, doi:10.2144/0000113878 (2012).

2 Zheng, G. X. *et al.* Massively parallel digital transcriptional profiling of single cells. *Nature communications* **8**, 14049, doi:10.1038/ncomms14049 (2017).

3 Satija, R., Farrell, J. A., Gennert, D., Schier, A. F. & Regev, A. Spatial reconstruction of single-cell gene expression data. *Nature biotechnology* **33**, 495-502, doi:10.1038/nbt.3192 (2015).

4 Macosko, E. Z. *et al.* Highly Parallel Genome-wide Expression Profiling of Individual Cells Using Nanoliter Droplets. *Cell* **161**, 1202-1214, doi:10.1016/j.cell.2015.05.002 (2015).

5 Butler, A., Hoffman, P., Smibert, P., Papalexi, E. & Satija, R. Integrating single-cell transcriptomic data across different conditions, technologies, and species. *Nature biotechnology*, doi:10.1038/nbt.4096 (2018).

6 Finak, G. *et al.* MAST: a flexible statistical framework for assessing transcriptional changes and characterizing heterogeneity in single-cell RNA sequencing data. *Genome biology* **16**, 278, doi:10.1186/s13059-015-0844-5 (2015).

7 Subramanian, A. *et al.* Gene set enrichment analysis: a knowledge-based approach for interpreting genome-wide expression profiles. *Proceedings of the National Academy of Sciences of the United States of America* **102**, 15545-15550, doi:10.1073/pnas.0506580102 (2005).

8 Reimand, J. *et al.* Pathway enrichment analysis and visualization of omics data using g:Profiler, GSEA, Cytoscape and EnrichmentMap. *Nature protocols* **14**, 482-517, doi:10.1038/s41596-018-0103-9 (2019).

9 Kucera, M., Isserlin, R., Arkhangorodsky, A. & Bader, G. D. AutoAnnotate: A Cytoscape app for summarizing networks with semantic annotations. *F1000Research* **5**, 1717, doi:10.12688/f1000research.9090.1 (2016).

10 Kirouac, D. C. *et al.* Dynamic interaction networks in a hierarchically organized tissue. *Molecular systems biology* **6**, 417, doi:10.1038/msb.2010.71 (2010).

11 Uhlen, M. *et al.* Proteomics. Tissue-based map of the human proteome. *Science* **347**, 1260419, doi:10.1126/science.1260419 (2015).

12 Razick, S., Magklaras, G. & Donaldson, I. M. iRefIndex: a consolidated protein interaction database with provenance. *BMC bioinformatics* **9**, 405, doi:10.1186/1471-2105-9-405 (2008).

13 Cerami, E. G. *et al.* Pathway Commons, a web resource for biological pathway data. *Nucleic acids research* **39**, D685-690, doi:10.1093/nar/gkq1039 (2011).

14 Stark, C. *et al.* BioGRID: a general repository for interaction datasets. *Nucleic acids research* **34**, D535-539, doi:10.1093/nar/gkj109 (2006).

15 Soumillon, M., Cacchiarelli, D., Semrau, S., van Oudenaarden, A. & Mikkelsen, T. S. Characterization of directed differentiation by high-throughput single-cell RNA-seq. *bioRxiv*, 003236 (2014).

16 Derr, A. *et al.* End Sequence Analysis Toolkit (ESAT) expands the extractable information from single-cell RNA-seq data. *Genome research* **26**, 1397-1410, doi:10.1101/gr.207902.116 (2016).

17 Dobin, A. *et al.* STAR: ultrafast universal RNA-seq aligner. *Bioinformatics* **29**, 15-21, doi:10.1093/bioinformatics/bts635 (2013).

18 Li, H. *et al.* The Sequence Alignment/Map format and SAMtools. *Bioinformatics* **25**, 2078-2079, doi:10.1093/bioinformatics/btp352 (2009).

19 Anders, S. & Huber, W. Differential expression analysis for sequence count data. *Genome biology* **11**, R106, doi:10.1186/gb-2010-11-10-r106 (2010).

20 Love, M. I., Huber, W. & Anders, S. Moderated estimation of fold change and dispersion for RNA-seq data with DESeq2. *Genome biology* **15**, 550, doi:10.1186/s13059-014-0550-8 (2014).

21 Livak, K. J. & Schmittgen, T. D. Analysis of relative gene expression data using real-time quantitative PCR and the 2(-Delta Delta C(T)) Method. *Methods* **25**, 402-408, doi:10.1006/meth.2001.1262 (2001).

22 Eisenberg, E. & Levanon, E. Y. Human housekeeping genes, revisited. *Trends in genetics : TIG* **29**, 569-574, doi:10.1016/j.tig.2013.05.010 (2013).
23 Sharma, K. *et al.* Cell type- and brain region-resolved mouse brain proteome. *Nature neuroscience* **18**, 1819-1831, doi:10.1038/nn.4160 (2015).
24 Tabula Muris, C. *et al.* Single-cell transcriptomics of 20 mouse organs creates a Tabula Muris. *Nature* **562**, 367-372, doi:10.1038/s41586-018-0590-4 (2018).
25 Kantzer, C. G. *et al.* Anti-ACSA-2 defines a novel monoclonal antibody for prospective isolation of living neonatal and adult astrocytes. *Glia* **65**, 990-1004, doi:10.1002/glia.23140 (2017).
26 Zeisel, A. *et al.* Molecular Architecture of the Mouse Nervous System. *Cell* **174**, 999-1014 e1022, doi:10.1016/j.cell.2018.06.021 (2018).
27 Boisvert, M. M., Erikson, G. A., Shokhirev, M. N. & Allen, N. J. The Aging Astrocyte Transcriptome from Multiple Regions of the Mouse Brain. *Cell reports* **22**, 269-285, doi:10.1016/j.celrep.2017.12.039 (2018).
28 Clarke, L. E. *et al.* Normal aging induces A1-like astrocyte reactivity. *Proceedings of the National Academy of Sciences of the United States of America* **115**, E1896-E1905, doi:10.1073/pnas.1800165115 (2018).
29 Soreq, L. *et al.* Major Shifts in Glial Regional Identity Are a Transcriptional Hallmark of Human Brain Aging. *Cell reports* **18**, 557-570, doi:10.1016/j.celrep.2016.12.011 (2017).
30 Carpenter, A. E. *et al.* CellProfiler: image analysis software for identifying and quantifying cell phenotypes. *Genome biology* **7**, R100, doi:10.1186/gb-2006-7-10-r100 (2006).
31 Xu, H., Chen, M., Manivannan, A., Lois, N. & Forrester, J. V. Age-dependent accumulation of lipofuscin in perivascular and subretinal microglia in experimental mice. *Aging cell* **7**, 58-68, doi:10.1111/j.1474-9726.2007.00351.x (2008).
32 Mann, H. B. & Whitney, D. R. On a Test of Whether one of Two Random Variables is Stochastically Larger than the Other. *Ann Math Statist* **18**, 50-60, doi:10.1214/aoms/1177730491 (1947).
33 Benjamini, Y. & Hochberg, Y. Controlling the False Discovery Rate: A Practical and Powerful Approach to Multiple Testing. *Journal of the Royal Statistical Society. Series B* **57**, 289-300 (1995).